Experimental investigation of efficient and simple wind-turbine based on DFIG-direct power control using LCL-filter for stand-alone mode

Bruno Francois, Fayssal Amrane, Chaiba Azeddine

Experimental Investigation of Efficient and Simple Wind-Turbine based on DFIG-Direct Power Control using LCL-Filter for Stand-alone Mode

Keywords

«Wind Energy Conversion System: WECS», «Direct Power Control: DPC», «LCL-Filter», «dSPACE 1103», «Doubly Fed Induction Generator: DFIG», «Integral-Proportional: IP».

Abstract

This paper suggests an experimental implementation study of the Wind Energy Conversion System (WECS) based on efficient Direct Power Control (DPC). Stand-alone mode for variable wind speed application using Doubly-Fed Induction Generator (DFIG) is studied and developed in this work. Due to the wind power performance limitation of traditional PI controllers, such as overshoot, response time, and static error; IP (integral-Proportional) controllers is replaced instead of the PI to control rotor current d-q components (I_{rd} and I_{rq}) in a Park frame through AC-DC-AC converter. A comparative experimental study was implemented to improve the power quality using L, LC & LCL passive filters between the DFIG's rotor circuit and the inverter. Experimental results prove that the proposed DPC under stand-alone mode with LCL-Type filter could operate in several conditions despite the sudden wind speed variations. It improves the unity power factor grid operation (≈0.98), dynamic responses, and the decoupled power control with high wind power performances: good reference tracking, short response time, neglected overshoot, and low power error. The power quality injected into the RL-load satisfied the limit specified by IEEE harmonic standard 519 (less than 5%).

1. Introduction

Wind power potential has been rising massively in the recent years, with new plants by 2050, capacity of 5044 (GW) for onshore wind turbines and capacity of 1000 (GW) for offshore wind turbines [1]. Wind power generation is considered as one of the most efficient alternative sources of electricity due to its economic advent ages. [2]. For a variable speed wind turbine (VSWT), there are multiple benefits to the use of a double-fed induction generator (DFIG), such as decreased noise, lower mechanical stress on the wind generator shaft, scaled-down inverters, and the ability to regulate stator active and reactive power [3, 5]. The principal gain is that the power converter is rated at only 25-30% of the generator power (Fig.1), which reduces the price of the converter and the power losses [6, 8]. It also permits control of reactive and active power. The power electronics became a lot of advanced with the increasing capability coverage, and have brought important performance

enhancements to wind turbines (WTs); not solely increasing energy and reducing mechanical stress [9], but also by allowing the WTS to operate as a more flexible controllable generator for incorporation into electrical networks.

The major AC power generation-based DFIG control topologies for both grid-connected [10, 12] and stand-alone [13, 17] systems are largely provided in the existing research literature (please refer Fig.1). The following are the more popular control approaches, for the control of DFIGs, field-oriented control (FOC) through stator flux based, and Direct Power Control (DPC). In [18-19], DPC is known for its fast time-to-response, easy structure, and less parameter reliance, which has attracted a wide range of academic and industrial communities.

In [20], the authors have studied a novel algorithm for DC-voltage tuning. The basic idea of this research focused on the adjustment of the DC link voltage is carried out by means of the stator voltage magnitudes control through a d-axis rotor current of the flux control loop in a Park frame. The load current will be immediately assisted by the q-axis rotor current.

In [21], the authors suggested an interessant search called «sensorless frequency and voltage control" in autonomous mode. The basic goal of this paper was to minimize the number of detectors and the detectorless realization was adopted to achieve the field orientation and adjust DC-voltage and the stator frequency.

In [22], the authors proposed a new study to analyze an autonomous DFIG system and the DC voltage control with sensors reduction. The aim of this search is a redesigned regulation diagram for an autonomous DFIG, which does not rely on the measurement of the stator voltages and currents. The nonlinear nature of the wind system requires the addition of filters to reduce current ripples, especially between the power electronic converter, the generator rotor circuits, and the grid.

Generally, in order to smooth the output currents from a Voltage Source Inverter (VSI); higher order filters such as: LCL and LLCL will replace the traditional L-filter [23-24].

Due to these merits, this solution is now widely used in distributed renewables generation [25-26] and active power filters.

The significant contributions are as follows:

1. Robust d-q axis rotor-current IP controllers based DPC for WECS-DFIG in the Standalone mode is experimentally tested and validated under hard working conditions, to demonstrate the feasibility and effectiveness of the proposed control.
2. The enhancement of the quality of the power delivered to the RL load is verified and approved by the experiment tests (using the LCL type-filter between the rotor circuit of the DFIG and the DC-AC converter).
3. Simplified implementation, reduced switching loses, high dynamic response and strong follow-up powers are the most significant achievements of the suggested control system.

4. The proposed power control displays high performance of the wind power system in both the steady and transient states.

This paper is structured as follows: first, the suggested control (standalone topology) is discussed in Section 2. Then, the turbine design, the description of the MPPT strategy with simulation results, the modeling of the grid-side converter and the DFIG are respectively illustrated in Section 3. In Section 4, the proposed rotor-side converter (RSC) is demonstrated with a comparative study between both: the PI controller and the robust IP controller. On the other hand, a complete hardware implementation (turbine emulator + DFIG) using dSPACE1103 is shown in detail. In section 5, the influence of filters (L, LC and LCL) on the power quality of the wind system will be illustrated and explained with experimental results. In section 6, the simulation and experimental results are shown and discussed with more detailed explanations. Finally, the reported work is concluded.

2. Proposed Control (stand-alone topology)

In the WECS review, there are basically two DFIG stator-connection topologies.

Firstly, the stator-circuit is connected to the grid, this topology known as Grid-connected [5-12].

NB: Before the Stator-grid connection it should be respecting the synchronization criteria's between the stator and grid):

1- Same frequency ($f_{grid} = f_{stator}$).
2- Same voltage magnitude ($U_{grid} = U_{stator}$),
3- Same sequence order (123=UVW)
4- Zero voltage angle phase ($\boldsymbol{\theta}$=0°)

Secondly, the stator-circuit of the DFIG is connected directly to the RL-load via the capacitors-bank to provide a micro-grid, this topology known by the stand-alone [13-22]. The main hardware advantage of this topology compared to the first one; is that it doesn't require the synchronization device between the stator-circuit and the RL-load. In order to provide the power to the grid by the means of the rotor, the RSC is controlled via the DPC by the means of IP regulator under d-q axis rotor currents "I_{rd} and I_{rq}", to generate the PWM switching signals to control the inverter.

The generator speed varies near the synchronous speed (1500 rpm) in the stable zone; because the electromagnetic torque as a function of the rotation speed is in the straight-line geometric form, which provide directly the electromechanical parameters of the wind power system and consequentely the rotor power values which are resepectively absorbed / or injected into the network.

So, if the DFIG-rotation speed is below 1500 rpm; means that the slip will take a positive value s=(ns-n)/ns>0 ⇒ so the DFIG drives in Sub-synchronous mode ⇒ the rotor absorbs the power from the grid (Pr=s*Pn) by the means of the PWM Back-to-back (B-2-B) converter.

And if the DFIG-rotation speed is above 1500 rpm; the slip will take negative value s=(ns-n)/ns<0 ⇒ so the DFIG operates in Super-synchronous mode ⇒ the rotor delivers the power to the grid (Pr=s*Pn) via the B-2-B converter.

Fig.2 presents the proposed Stand-alone power-control scheme. An LCL-type filter is connected between the DFIG's rotor-circuit and the inverter to improve the stator and rotor voltage waveforms.

The objective is to ensure high performances of the suggested control under robustness currents/speed tests in terms of good tracking, small overshoot, short response time, low current and power error.

To guarantee this kind of performance regarding current references and speed fluctuations, IP (Integral-Proportional) controllers are designed to regulate the rotor current components Ird and Irq under the d-q axis.

3. WECS Mathematical Model

3.1 Wind turbine mathematical model

The wind turbine input power is expressed as [12-14]:

$$P_v = \frac{1}{2} * \rho * S_w * v^3 \quad (1)$$

Where ρ represents the density of the air; S_w is the area swept by the blades of the wind turbine; v is the wind speed.

The mechanical power output of the wind turbine (the schematical diagram is illustrated in Fig.3) is expressed as follows:

$$P_m = C_p * P_v = \frac{1}{2} * C_p * \rho * S_w * v^3 \quad (2)$$

Where the power coefficient (Cp) refers to the energy conversion efficiency of the wind turbine (as shown in Fig.4). Cp is a nonlinear function of Tip Speed Ratio (TSR or λ) and blade angle β [°].

λ is determined as the relationship between the tip speed of the wind turbine blades to the wind speed. λ is defined as :

$$\lambda = \frac{R * \Omega_t}{v} \quad (3)$$

Where R is the radius of the blade, Ω_t is the angular velocity of the turbine.

The expression for C_p (λ, β) may be described as below [12-14]:

$$C_p(\lambda, \beta) = \left(0.5 - 0.0167 * (\beta - 2)\right) * \sin\left[\frac{\pi * (\lambda + 0.1)}{18.5 - 0.3 * (\beta - 2)}\right] - 0.00184 * (\lambda - 3) * (\beta - 2) \quad (4)$$

The MPPT strategy with no wind speed measurement is shown in Fig.5; therefore, P_{s_ref} (stator reference power) is computed by the multiplying the MPPT output (the mechanical speed Ω_{mec}) and the electromagnetic torque T_{em_ref}; this provides $P_{s\_ref} = \Omega_{mec} * T_{em\_ref}$.

By employing MATLAB/Simulink® to plot the curve of the power coefficient (C_p) under various tilt angles (B°) as depicted in Fig.6, it is evident that the null pitch angle (B°=0°) provides the greatest C_p, which corresponds to the optimum top speed ratio (TSR). Fig.7 shows the 3-Dimensional characteristics of C_p as a function of TSR and tilt angles (B°) respectively. The main objective of the MPPT strategy is to adjust the wind turbine speed to the wind speed, in such a way as to maximize the converted power, thus improving its energy efficiency and integration with the RL-load.

Two wind speed profiles are proposed (are used later in Section.6.1), as shown in Fig.8 (the upper side) shows the simulation results in the case of stepped wind speed, and the underside displays the simulation results with random wind speed. It can be observed that the maximum value of C_p (C_{p_max}=0.4785) is attained for B°=0° and at λ_{Opt}=8.098.

This working point refers to the maximum power point tracking (MPPT) [14], as shown in Fig.8 (the upper left side of the two proposed cases). Then, the robustness of the MPPT algorithm is tested by considering the proposed wind speed profiles. As a result (Fig.8), the greatest value of the C_p in (C_{p_max}= 0.4785) is reached regardless of the suddenly changing wind speed.

T_{aero}, $T_{gearbox}$, and T_{em} are shown in Fig.8 (bottom) for the two suggested wind profiles respectively. Tem becomes negative in the generator mode. Fig.9 shows the whole circuit topology of a DFIG system with a back-to-back PWM converter. In the next sections, the GSC (Grid Side Converter), an RSC (Rotor Side Converter), and a DC-link are modeled and discussed in detail.

3.2 Mathematical model of DFIG

The dynamical model of the DFIG can be represented by the subsequent equations of state in the synchronized reference frame [1-2], knowing that the d-axis is lined up with the stator flux vector, as shown in Fig.10 [19-20].

- Stator and rotor voltages:

$$V_{sd} = R_s * I_{sd} + \frac{d}{dt}\Phi_{sd} - \omega_s * \Phi_{sq}. \quad (5)$$

$$V_{sq} = R_s * I_{sq} + \frac{d}{dt}\Phi_{sq} + \omega_s * \Phi_{sd}. \quad (6)$$

$$V_{rd} = R_r * I_{rd} + \frac{d}{dt}\Phi_{rd} - (\omega_s - \omega_r) * \Phi_{rq}. \quad (7)$$

$$V_{rq} = R_r * I_{rq} + \frac{d}{dt}\Phi_{rq} + (\omega_s - \omega_r) * \Phi_{rd}. \quad (8)$$

- Stator and rotor fluxes:

$$\Phi_{sd} = L_s * I_{sd} + L_m * I_{rd}. \quad (9)$$

$$\Phi_{sq} = L_s * I_{sq} + L_m * I_{rd}. \quad (10)$$

$$\Phi_{rd} = L_r * I_{rd} + L_m * I_{sd}. \quad (11)$$

$$\Phi_{rd} = L_r * I_{rd} + L_m * I_{sd}. \quad (12)$$

- The electromagnetic torque is given by:

$$T_{em} = p * L_m * (I_{rd} * I_{sq} - I_{rq} * I_{sd}). \quad (13)$$

- And its associated motion equation is:

$$T_{vis} = f * \Omega_{mec}. \quad (14)$$

$$T_{em} - T_r = J * \frac{d}{dt}\Omega_{mec} + T_{vis}. \quad (15)$$

$$J = \frac{J_{turbine}}{G^2} + J_g. \quad (16)$$

Where; R_s, R_r, L_r, and L_s are respectively the resistances and the inductances of the stator and of the rotor circuit and L_m is the mutual inductance, σ is the leakage factor: $\sigma = 1 - \frac{L_m^2}{L_s * L_r}$. V_{sd}, V_{sq}, V_{rd}, V_{rq}, I_{sd}, I_{sq}, I_{rd}, I_{rq}, Φ_{sd}, Φ_{sq}, Φ_{rd} & Φ_{rq} respectively represent the components along with the d and q axis of the stator and rotor voltages, currents and flux. T_{em}, T_r, T_{vis}, T_{aero}, and $T_{gearbox}$ are the electromagnetic, load, viscous, aerodynamic, and gearbox torques. J_g, $J_{turbine}$, and J are respectively the generator, turbine and total inertia, Ω_{mec} is the mechanical speed, and G: is the gain of gearbox. p is the number of pole pairs, ω_s is the stator pulsation = 314 rad/s, ω_r is the rotor pulsation, ω_{slip} is the slip pulsation $=(\omega_s - \omega_r)$ and f is the friction coefficient. T_s and T_r are stator and rotor time-constants with: $T_r = \frac{L_r}{R_r}$; $T_s = \frac{L_s}{R_s}$; s is the slip. $s = \frac{\omega_s - \omega_r}{\omega_s}$ and $\omega_s - \omega_r = s * \omega_s$.

3.3 Grid Side Converter (GSC) and DC-link voltage control [27, 29]:

Although some back-to-back PWM converter DC link voltage control schemes have been studied [26-27]. In DFIG's back-to-back PWM converter, the bidirectional power is transmitted between the GSC and the RSC.

Fig.11 displays the configuration of the GSC. Assuming the equilibrated grid voltages, we achieve the following relationships:

$$\begin{cases} V_{1N} = \frac{1}{3} * (+2 * V_1 - V_2 - V_3) \\ V_{2N} = \frac{1}{3} * (-V_1 + 2 * V_2 - V_3). \\ V_{3N} = \frac{1}{3} * (-V_1 - V_2 + 2 * V_3) \end{cases} \quad (17)$$

Depending on whether the switches T_{ij} are closed or open, the voltages at the terminals of the V_i branch may be equal to V_{dc} or 0. The switching states S_{11}, S_{12} and S_{13} are given and are set to 1 if the switch T_{ij} is closed or to 0 if it is blocked. Then, the equation system (17) can be re-written as follows:

$$\begin{pmatrix} V_{1N} \\ V_{2N} \\ V_{3N} \end{pmatrix} = \frac{V_{dc}}{3} * \begin{pmatrix} +2 & -1 & -1 \\ -1 & +2 & -1 \\ -1 & -1 & +2 \end{pmatrix} * \begin{pmatrix} S_{11} \\ S_{12} \\ S_{13} \end{pmatrix} \quad (18)$$

The rectified current may be written as below:

$$I_{rec} = I_{dc\_GSC} = S_{11} * I_{ga} + S_{12} * I_{gb} + S_{13} * I_{gc} \quad (19)$$

In this part, the switching signals are established by means of a comparison (using hysteresis regulators) between the measured network currents I_{g_abc} and the reference network currents $I^*_{g\_abc}$. The DC voltage across the capacitor is calculated by:

$$C * \frac{dV_{dc}}{dt} = I_c = I_{rec} - I_f = (S_{11} * I_{ga} + S_{12} * I_{gb} + S_{13} * I_{gc}) - I_f. \quad (20)$$

Fig.12 shows the control block schematic of a vector control (VC) for the GSC. This PWM converter is used to maintain the DC link voltage at a fixed value.

The GSC is generally controllable by a VC strategy with the orientation of the grid voltage. This voltage reference frame is defined by the d-q axis, which permits decoupling the expression of reactive and active power transferred between the rotor side and the grid.

The DC link voltage is expressed as follows:

$$V_{dc}^{*} = V_{dc\_meas} + \frac{1}{C_{dc}}\int_{0}^{t} i_{dc}dt = V_{dc\_meas} + C * \frac{1}{C_{dc}}\int_{0}^{t}(i_{dc\_GSC} - i_{dc\_RSC})dt \quad (21)$$

Where i_{dc_RSC} and i_{dc_GSC} are the DC current flowing into or out of the RSC and GSC, respectively, and i_dc is the capacitor charging current. A DC capacitor is used to suppress undulations and maintain the DC link voltage relatively flat.

Consequently, a hysteresis controller is employed in which the error between the targeted and the real currents is transmitted by a controller [28]. The gain settings (K_{P_DC} and K_{I_DC}) of the bus voltage controller are listed in the Appendix section (Table.24). A fig.13 show the hysteresis band is used to drive the rectifier IGBT's using the grid current comparator. We can also see the impact of the hysteresis band in the THD of the injected current.

4 Rotor Side Converter (RSC): Improved Direct Power Control (DPC) using IP controllers

Supposing the stator winding resistance Rs is neglected. The voltage and flux equations of the stator windings can be summarized as below [13]:

$$V_{sd} = 0 \quad (22)$$

$$V_{sq} = V_s \cong \omega_s . \Phi_s \quad (23)$$

$$\Phi_s = L_s . i_{sd} + L_m . i_{rd} \quad (24)$$

$$0 = L_s . i_{sq} + L_m . i_{rq} \quad (25)$$

From eq. (09) and (10), the equation relating the stator currents to the rotor currents is calculated as follows:

$$i_{sd} = \frac{\Phi_s}{L_s} - \frac{L_m}{L_s} . i_{rd} \quad (26)$$

$$i_{sq} = -\frac{L_m}{L_s} . i_{rq} \quad (27)$$

The active and reactive powers of the stator are defined as:

$$P_s = V_{sd} . i_{sd} + V_{sq} . i_{sq} \quad (28)$$

$$Q_s = V_{sq} . i_{sd} - V_{sd} . i_{sq} \quad (29)$$

Considering the selected frame of reference, the upper power equations may be written as shown below:

$$P_s = V_s . i_{sq} \quad (30)$$

$$Q_s = V_s . i_{sd} \quad (31)$$

By substituting the stator currents with their corresponding expressions (26) and (27), we can obtain the following expressions:

$$P_s = -V_s . \frac{L_m}{L_s} . i_{rq} \quad (32)$$

$$Q_s = \frac{V_s^2}{\omega_s * L_s} - V_s . \frac{L_m}{L_s} . i_{rd} \quad (33)$$

On the other side, the electromagnetic torque expression is equal to:

$$T_{em} = P * \left(\frac{L_m}{L_s}\right) * \Phi_{sd} * I_{rq} . \quad (34)$$

Fig.14 depicts the simple model of the DFIG, which is built on the orientation of the stator flux vector. The regulation of the DFIG across the DC-AC converter connected to its rotor circuits must guarantee the needed torque to vary the mechanical generator speed (Ω_{mec}) to extract the maximum power, by enforcing the appropriate rotor voltages to the DFIG [27]. The reactive power target is generally equal to zero for the MPPT control strategy. From eq. (33), the torque can be controlled by acting on the rotor quadrature current component (Irq) of the DFIG, so we can deduce the current reference I_{rq}^* for a desired torque T_{em}^*.

$$I_{rq}^* = -\frac{L_s}{P.L_m.\Phi_s} * T_{em}^* \tag{35}$$

Fig.(13 and 14) show the stator/rotor flux vectors in the d-q synchronous frame and the simplified doubly-fed induction generator model, respectively. Similarly, the rotor d-axis component (Ird) is employed to control the reactive power (eq. 36).

Therefore, we can write the subsequent equations (the relationship between the Irdq and the powers "Ps and Qs" [27]:

$$I_{rd}^* = \frac{\Phi_s}{L_m.} - \frac{L_s}{V_s.L_m} * Q_s^* \tag{36}$$

$$I_{rq}^* = -\frac{L_s}{P.L_m.\Phi_s} * T_{em}^* = \frac{L_s}{V_s.L_m} * P_s^* \tag{37}$$

Considering that eqs. "35 & 37" are in fact the same ones that depend respectively on the torque or on the active power.

Unlike the MPPT control strategy where the quadrature (or transverse) reference component I_{rq}^* is the image of the torque to be provided, the power controller of this algorithm calculates and sends to its output the q-d axis components (I_{rq}^* and I_{rd}^*) of the DFIG, which are in proportion to the active and reactive power of the stator respectively. They are obtained from equations (35) and (36) respectively. (35) & (36).

In the next steps, PI and IP regulators are suggested to regulate the Irq and Ird currents respectively (Fig.16). The IP regulators are similar to the PI regulators, except that the proportional and integral actions are serialized unlike the PI regulators (where these actions are paralleled) (Fig.15-(a and b) respectively).

4.1 Brief difference between PI and IP controllers:

Both the PI and IP controllers (Fig.15 a-b) have proportional and integral gains, but both of them are architecturally and operationally dissimilar. The IP regulator is a twin-loop control diagram in which the proportional gain K_p and integral gain K_i values are looped together to provide certain features to the control loop, which the traditional PI regulator does not provide. Also, every gain value has its own significance in the process of control, and the gain values are tuned to obtain the required response. The IP controller can also be known as a double-loop PI controller.

The proportional gain of a regulator generates an output in proportion to the current error value. For a significant variation in the error value, a similar change in the output occurs. A

large proportional gain yields an imbalance in the system, whereas a low proportional gain makes the system less sensitive. Likewise, with a lower proportional gain, the control action may become too low when reacting to system perturbations. The P-only controller, when employed, cannot fully remove the steady-state error. But a PI controller can readily accomplish this.

Obviously, the IP controller has 02 separate loops with an integral gain and a proportional gain in the return path. Again, in this situation, an error signal is produced by comparison of the reference signal and the output signal, which is then applied to the integral gain. The output of this is again compared to the output signal multiplied by the proportional gain. The resulting signal is further treated to provide control signals to trigger the converter switch.

The arrangement of cascaded proportional and integral gains in the PI controller results is shown in Fig.15-b, is determined by the addition of an extra zero to the transfer function of the overall system. The impact of the zero is to contributing a marked early peak to the system performance and a higher percentage of overshoot. This can be demonstrated as follows.

$$PI = K_p + \frac{K_i}{S} = \frac{(K_p * S + K_i)}{S} \tag{38}$$

Therefore, it is clear from the above formula that the PI controller inserts a left negative half-plane on the real axis which has the value K_i/K_p. If the zero amplitude is low, its location will be nearer the origin, which will improve the spike phenomenon. When the K_p value is raised to enhance the response time of the system, the value of the zero becomes lower and gets increasingly nearer to the origin, which causes overshoot. The previously discussed problem is averted in the case of the IP controller (Fig.15-a).

The multi-loop assembly prevents the insertion of an extra zero in the system. This reduces the overshoot percentage in the system response. As a result, the IP controller (Fig.15-a) can be readily adjusted to obtain a better transient response. An abrupt rise or fall in input values can frequently adversely affect the output of the system. A suitable controller must continue to carry out its control action with no deviation from the previous value. Therefore, the adjustment of the dual loop gain value in an IP controller enhances the dynamic response of the system drastically compared to the PI controller.

4.2 Conventional Proportional Integral (PI) regulators applied in DPC

The open-loop transfer function (OLTF) with the controllers is written in the following way (knowing that: “s” is Laplace variable):

$$OLTF = \frac{output}{input} = \frac{V_{rdq}}{I_{rdq}} = \frac{s + \frac{K_{I\_PI}}{K_{P\_PI}}}{\frac{s}{K_{P\_PI}}} * \frac{\frac{L_m * V_s}{L_s * (L_r - \frac{L_m^2}{L_s})}}{s + \frac{L_s * R_r}{L_s * (L_r - \frac{L_m^2}{L_s})}} \tag{39}$$

To implement compensation, we set: $\frac{K_{I\_PI}}{K_{P\_PI}} = \frac{L_s * R_r}{L_s * (L_r - \frac{L_m^2}{L_s})}$ (***)

Then the *OLTF* is expressed as:

$$OLTF = \frac{K_{P\_PI} * \frac{L_m * V_s}{L_s * (L_r - \frac{L_m^2}{L_s})}}{S}. \quad (40)$$

And the closed loop transfer function (*CLTF*):

$$CLTF = \frac{1}{1+\tau_{cl} * S} \quad with \quad \tau_{cl} = \frac{1}{K_{P\_PI}} * \frac{L_s * (L_r - \frac{L_m^2}{L_s})}{L_m * V_s} \Rightarrow CLTF = \frac{1}{1+0.01 * S} \quad (41)$$

With τ_{cl} is the time constant of the system that is fixed at 10 ms corresponding to a satisfying fast dynamic according to the slow variations of the wind speed and the large mechanical constants time.

From eq. (41), we can determine the gains K_{P_PI} *and* K_{I_PI} according to the parameters of the machine and the response time:

$$\begin{cases} k_{P\_PI} = \frac{1}{\tau_{cl}} * \frac{L_s * \left(L_r - \frac{L_m^2}{L_s}\right)}{L_m * V_s} \\ k_{I\_PI} = \frac{1}{\tau_{cl}} * \frac{L_s * R_r}{L_m * V_s} \end{cases}. \quad (42)$$

4.3 The proposed Integral Proportional (IP) regulators applied in DPC

As described above, the system is first regulated by simplifying the system into a monovariable model. Thus the simplified model used for IP dimensioning is as flows (Fig.16-(a & b)), and the global proposed control scheme is described in Fig.16-(c). The closed loop transfer function (CLTF) with the proposed control scheme is described in Fig.16-(c). The closed loop transfer function (CLTF) with the

IP controller is then written:

$$CLTF = \frac{Output}{Input_{ref}} = \frac{k_{I\_IP} * k_{P\_IP} * A}{s^2 + (k_{P\_IP} * A + B)s + k_i * k_{P\_IP} * A}. \quad (43)$$

Such as: $\begin{cases} A = \frac{L_m * V_s}{L_s * L_r - L_m^2} \\ B = \frac{L_s * R_r}{L_s * L_r - L_m^2} \end{cases}$.

By identification with a second order system of transfer function:

$$CLTF = \frac{V_{rdq}}{I_{rdq}} = \frac{k * \omega_n^2}{s^2 + 2 * \xi * \omega_n * s + \omega_n^2}. \quad (44)$$

The gains of the correctors will be expressed as a function of the parameters of the machine as follows:

$$\begin{cases} k_{I\_IP} = \frac{\omega_n^2}{k_p * A} \\ k_{P\_IP} = \frac{2 * \xi * \omega_n - B}{A} \end{cases}. \quad (45)$$

Hence replacing A and B by their respective expressions we obtain (refer to Table.25):

$$\begin{cases} k_{I\_IP} = \frac{\omega_n^2 * (L_s * L_r - L_m^2)}{k_p * L_m * V_s} \\ k_{P\_IP} = \frac{2 * \xi * \omega_n * (L_s * L_r - L_m^2) - L_s * R_r}{L_m * V_s} \end{cases}. \quad (46)$$

The damping coefficient (known by "**ξ**") determines whether it has an attenuation or resonance to the natural pulsation. In this paper, we need an overshoot less than 5% (which

means a damping ratio ξ of greater than 0.7). If **ξ** ≥1, it notes that the rise time and response time increase with **ξ**. And for low values of **ξ** (**ξ** ≤ 0), the response time increases when **ξ** decreases because the magnitude of the oscillations increases and the transient regime is longer and longer. It is noted that the response time is minimum for **ξ**≈0.7, because it is beyond this value that the first overshoot is less than 5%. So the optimal compromise between damping and short response time is obtained for **ξ** = $\sqrt{2}/2$ ≈ 0.707. As for the dynamics of the system (ω_n), it will be chosen during the simulation in order to have the best performances. It can be seen that the conventional DPC based on 1st order Transfer function, and the proposed DPC based on 2nd order transfer fucntion.

In the next section, the stability of each closed loop TF is studied using "Bode Plot"

4.4 Stability study using Root Locus Transfer function

Frequency responses analysis is a key to understanding and performance properties of control systems.

Bode plots is way applied to plot and analyze the frequency response of a studied system. The above transfer function (TF) is expressed in terms of magnitude and angle phase margins.

Fig.17 illustrates Frequency responses analysis of the conventional and proposed DPC control using Bode plot. The improvement rapidity and stability is adopted using the proposed control. The proposed control offers a higher damp magnitude/phase than the conventional one. The Interpretation of the Bode diagram (conventional DPC and proposed DPC respectively; Fig.17-(a & b)):

a- Bandwidth (response time):

According to Fig.17-(a and b) the bandwidth of the proposed control (IP) is wider compared to that of the conventional control (PI) equal respectively: 80 (Hz) and 6 (Hz), which reflects the speed which equals nearly 13.34 times of the proposed one than the conventional in the steady-state.

b- Phase margin (stability performance):

Fig.17-(a and b) illustrates the phase margin, which is equal to 120° for the proposed control (based on IP) is relatively less than that of the conventional control (based on PI) equal to 150 °. The phase margin reflects the robustness to the stability, which means that the proposed algorithm is less preferment in terms of stability than the conventional one. On the other side and in order to guarantee the system stability, different parameter variation cases are calculated and checked. Regardless of the hard work conditions, the system always keeps a wide phase margin which proves the high system stability. Knowing that the phase margin is calculated between the break of the zero (0) magnitude (in dB) and by projecting below which is appropriate in phase (in degree °).

c- <u>Stability verification test (by the means of sudden DFIG-parameters variation):</u>

The poles compensation method (*refer to equation-39*) witch eliminate the zero from the transfer function is always pull to the left-half plane regardless of the DFIG-parameters (**R_r, L_s, L_r** & **L_m**) variation : the stability is validated if and only if this function is always checked (correct): $\boxed{\frac{K_I}{K_P}=\frac{L_s*R_r}{L_s*\left(L_r-\frac{L_m^2}{L_s}\right)}}$(***)

In order to guarantee that the transfer function already pull to the left-half plane even if DFIG-parameters abrupt change, the real part of the pole should be negative ⇒$\boxed{s=-\frac{L_s*R_r}{L_s*\left(L_r-\frac{L_m^2}{L_s}\right)}}$, we know that this term (L_s* R_r) is always positive, it remains that the denominator should be positive: $\boxed{L_r-\frac{L_m^2}{L_s}>0}$⇒ $\boxed{L_r>\frac{L_m^2}{L_s}}$,

Case 01 (form table.20):
(L_r=0.1558)> (L_m^2/L_s=(0.15²/0.1554)=0.1448) ⇒ 0.1558>0.1448 is verified
Case 02 (+25% from L_m, L_s & L_r):
(+25%*L_r=0.1947)> (+25%*(L_m^2/L_s)=(0.1875²/0.1942)=0.181) ⇒ 0.1947>0.181 is verified
Case 03 (-25% from L_m, L_s & L_r):
(-25%*L_r=0.1168)> (-25%*(L_m^2/L_s)=(0.1125²/0.1165)=0.1086) ⇒ 0.1168>0.1086 is verified
Case 04 (+50% from L_m, L_s & L_r):
(+50%*L_r=0.2337)> (+50%*(L_m^2/L_s)=(0.225²/0.2331)=0.2172) ⇒ 0.2337>0.2172 is verified
Case 05 (-50% from L_m, L_s & L_r):
(-50%*L_r=0.0779)> (-50%*(L_m^2/L_s)=(0.075²/0.0777)=0.07239) ⇒ 0.0779>0.07239 is verified

<u>NB:</u>
Experimentally, the inductances (Lm, Ls, Lr) variation is relatively the same in terms of percentage (%), it is impossible that one inductance varies (Exp: Lm) and the others do not vary!!! (There is an electromagnetic link between them).

The response time (the algorithm speed) and the stability robustness are two contradictory quantities in electrical systems which present a dilemma in the majority of situation, and it is all quite normal that the proposed algorithm is strong in one criterion and a little strong in another. In our case, we tried to find the best compromise between these two quite important criteria especially in the performances in wind power systems. On the other side, the experimental results provided by different tests can later confirm this conclusion.

The previous section is proposed in order to make relationship between stability demonstration and simulation results, also to show the impact of the stability procedure in Wind-turbine system. For the detailed simulation study is proposed later (refer to Section 6).

Fig.18-(a and b) presents simultaion results of the Stator active' and reactive' powers under IDPC using PI and IP controllers (to control I_{rq} & I_{rd}) respectively. Fig.18-(a) illustrates the the behavior of stator active measured power (using PI and IP respectively) in steady and transient states in the period of 1.5 (sec).

The performances of the stator active power (zoom) using IP controllers is more powerful in terms of good tracking, very short response time and neglected overshoot despite the

sudden variation of the stator active reference power, in the inverse case, in stator active power using the PI controler; remarkables overshoot and power error are noted. Fig.18-(b) illustrates the behavior of stator reactive measured power (using PI and IP respectively) in steady and transient states in the period of 1.5 (sec). The stator reactive measured power (using IP controllers) follows exactely its reference (zoom) despite of the sudden variation the stator power reference, it can be seen improved performances using IP controller especially in tracking power, power error and response time.

Table.1 presents a brief comparative study using the simulation results of Fig.18. It is clear that the proposed power control based on IP is more robust than the conventional one using PI except the dynamic response which is faster in PI than IP. The analytical reason which prove that the overshoot is very smaller in power control topology using IP; is the absence of zero in transfer function of this one.

The analysis in S-domain shows that (PI) and (I-P) controllers have the same characteristic equations, and it can be seen that the zero introduced by the (P-I) controller is absent in the case of the (I-P) controller. Therefore the overshoot in the current for a step change in the input reference R(s), is expected to be smaller for the (I-P) controller.

4.5 Operating principle of DFIG

Although there are some limitations related to slip rings, the wound rotor induction machine has long been a preferred choice for wind power generators. Employing a suitable embedded strategy in the design of a WECS, the use of a slip-ring induction generator has been demonstrated to be economically attractive. Control of grid-connected and stand-alone variable speed wind turbines with a doubly-fed induction generator has been carried out and reported [31].

A wound rotor induction machine can work as a doubly-fed induction machine (DFIM) if a power converter is present in its rotor circuit. This converter drives the power flow into and out of the rotor windings. Because the DFIM can operates as a motor or generator at sub-synchronous and super-synchronous speeds, there are four operational modes in which the DFIM works.

The four different modes are illustrated in Fig. 19. When the machine operates over the synchronous speed, this operation is known as super-synchronous operation. In the same way, operation under the synchronous speed is known as sub-synchronous operation. In sub-synchronous and super-synchronous operation, the machine can be operated either as a motor or as a generator. In motor operation, the torque generated by the machine is positive.

On the other side, during generator operation, the machine requires mechanical input torque; therefore, the torque is negative during generator operation. The principle of a DFIM control in these modes can be understood more clearly by the power flow diagram given in

Fig.19. In this figure, P_s is the stator power, P_r is the rotor power and P_m is the mechanical power. When the DFIM operates as a motor in the sub-synchronous speed range (Fig.19-"1"), power is taken from the rotor.

This operating mode is usually named "slip-power recovery". If the speed rises so that the machine is operating at super-synchronous speeds (Fig.19), then the rotor power changes direction [31]. When the DFIM operates as a generator in the sub-synchronous speed range (Fig.19-"3"), power is supplied to the rotor. If the speed is increased so that the machine works at super-synchronous speeds (Fig.19-"4"), the rotor power changes direction once again. Since the machine will mainly operate as a generator for a wind energy application, running in Mode 3 and Mode 4 is more significant than Mode 1 and Mode 2. Nevertheless, for an ideal WECS system, all four operating modes are advisable. The motor modes are helpful when the generator is required to accelerate quickly to achieve the best operating speed and efficiency [31]. However, due to the high inertia of the wind generator drive train, the acceleration of the machine can be obtained by the torque of the wind itself. Therefore, motorization operations can be sacrificed if the system cost can be considerably decreased.

4.6 Emulator turbine control (Induction motor torque and flux control):

In proposed system drive, the induction motor imposes torque in electrical generator shaft according to a reference torque signal generated by wind turbine model from a reference wind speed. The whole motor induction torque and rotor flux control system is shown in Fig.20. The system includes closed loop stator current control with *PI* regulators with outer loop torque and rotor flux control. The torque control is realized by acting over the amplitude of the stator current and its frequency command is generated by the rotor flux control loop. Instead of constant rated flux, the reference rotor flux control loop can be programmed with the speed motor operation for efficient improvement. For torque and rotor flux calculation, stator current in *3-phase* system (*a, b and c*) is decomposed in two dimension orthogonal system (*α, β*) **[28].** This change of variables is well known as *Clarke transformation* and can be used to reduce the complexity of the system control implementation. After the acquisition, the stator '*abc'* voltage and current are transformed into a stationary *α-β* coordinate system. The voltage $V_{\alpha s}$ *is* aligned with the voltage V_{as} (*as shown in* Fig.20).

Then, the *αβ* stator voltages are calculated as:

$$V_{\alpha s} = \frac{1}{3}(V_{ab} - V_{ca}) \quad and \quad V_{\beta s} = \frac{\sqrt{3}}{3}V_{cb}) \tag{47}$$

The currents in *αβ* axes are calculated as:

$$I_{\alpha s} = I_{as} \quad and \quad I_{\beta s} = \frac{\sqrt{3}}{3}.(I_{as} + 2 * I_{bs}) \tag{48}$$

With the stator voltages and currents, the stator flux is calculated in the stationary *αβ* axes:

$$\Phi_{\alpha s} = \int (V_{\alpha s} - r_s * I_{\alpha s})dt \quad and \quad \Phi_{\beta s} = \int (V_{\beta s} - r_s * I_{\beta s})dt \tag{49}$$

The rotor flux in the stationary *αβ* axes can be calculated according to following equations:

$$\Phi_{\alpha r} = \frac{L_r}{L_m}.(\Phi_{\alpha r} - \sigma * L_s * I_{\alpha s}) \quad and \quad \Phi_{\alpha\beta} = \frac{L_r}{L_m}.(\Phi_{\beta r} - \sigma * L_s * I_{\beta s}) \tag{50}$$

4.7 Hardware implementation

In this section, the experimental wind-turbine emulator control has been presnted in order to explain the hardware relationship between the emulator turbine control (Degital Control Interface) and dSPACE1103 pannel via the wires connexion as schown in Fig.21.

Fig.22 illustrates the experimental tests bench developed in L2EP Laboratory. The different devices and mate-rials used are as follows;: 1: PC(with control desk interface to the right), 2: Oscilloscope, 3: dSPACE1103 panel, 4: PLL synchronization hardware, 5: Resistive load, 6: SEMIKUBE Driver Power supply (+24), 7: DC bus voltage SEMIKUBE (0 V-600 V) 8: Emulator turbine control (Rotor flux control), 9: DFIG (4.5 kW), 10: Emulator turbine /Induction motor (4 kW), 11: SEMIKUBE (Inverter), 12: Isolation card DC, 13: Current sensors, 14: Grid AC (0-400 V).

4.8 Inverter (SEMIKUBE) with R-L load under open loop using dSPACE1103 card

Before using the switching gates generated by the PWM algorithm to control rotor side converter (RSC) of the DFIG, it is necessary to test the SEMIKUBE (novel inverter version) in open loop with only R-L load under real time dSPACE1103 card, the isolation card developed in L2EP laboratory is illustrated in Fig.23.

Fig.24-(a) presents the hardware implementation of the proposed algorithm tests, to ensure the good performances of the SEMIKUBE using PWM strategy before feeding the rotor side converter (RSC) of DFIG.

As shown in Fig.24-(b), the signals switching 'S_n' are generated via isolation card (24 V/connector type HE10 DIN 41651, 34 contacts),. The different parameters used in this test are presented in details in Table.2. The power circuit of the three-phase voltage source inverter is obtained by adding a third leg to the single-phase inverter. Assuming that of the two power switches in each leg (phase) of the SEMIKUBE, one and only one is always on, that is, neglecting the time intervals when both switches
are off (blanking time), three switching variables, a, b and c can be assigned to the inverter.

A state of the inverter is assigned as 'abc', making for a total of eight states, from state 0, when all output terminals are clamped to the negative DC bus, through state 7 when they are clamped to the positive bus V_{dc_Test} (V). In this case, it is assumed that the R-L (resistive-inductive) load is three phases balanced load (the parameters tests are described in Table.2), the line to line voltage in each phase equals to:

$$\begin{pmatrix} V_{AB} \\ V_{BC} \\ V_{CA} \end{pmatrix} = R_{Load} * \begin{pmatrix} I_A \\ I_B \\ I_C \end{pmatrix} + L_{Load} * \frac{d}{dt}.\begin{pmatrix} I_A \\ I_B \\ I_C \end{pmatrix}. \tag{51}$$

$$I_A + I_B + I_C = 0 \tag{52}$$

The instantaneous line to line output voltages; $V_{AB}, V_{BA} and\ V_{CA}$ are given by:

$$\begin{pmatrix} V_{AB} \\ V_{BC} \\ V_{CA} \end{pmatrix} = \frac{1}{3} V_{dc} * \begin{pmatrix} +2 & -1 & -1 \\ -1 & +2 & -1 \\ -1 & -1 & +2 \end{pmatrix} * \begin{pmatrix} V_{AN} \\ V_{BN} \\ V_{CN} \end{pmatrix}. \tag{53}$$

Fig.24-(b) presents the PWM result and duty cycle of each leg inverter under *Matlab/Simulink® R2009b* software.

Fig.25 depicts the real photos of resistances and inductors for the proposed SEMIKUBE control tests are coupled together in star shape. Fig.26 illustrates the switching signals of the three (03) legs of the inverter; in high side (S_a, S_b and S_c) and low side (S_a', S_b' and S_c') with their zoom. Fig.27 displays the dead time between the switching signals (2 (µsec)) for each leg, for example the dead time between S_a and S_a' (leg 'a') equals to 2 (µsec) and the same thing in the rest of legs.

Fig.28 presents the load waveforms and their zoom under open loop topology. The top graph displays the current, simple and compound voltage and switching signal respectively in steady state and transient states. The fourth (04) bottom graphs represent only one cycle for each of them (2 (msec)*10= 1 cycle). It can be seen an excellent sinusoidal form of the load current (peak to peak load current equals to 4 (A)) with very neglected ripples.

5. Impact of Filters in RSC using the Fast Fourier Transform (FFT)

In order to choose an optimal filter topology for variable speed wind-turbines (VS-WT) to fed the DFIG's rotor via SEMIKUBE (inverter), parameters like efficiency, weight and volume have to be considered. Regarding efficiency, filter topologies with reduced losses are required, though those are relatively small when compared to losses in the inverter [30].

Weight and volume are considered as critical characteristics at offshore applications due to difficulties with transportation, installation and maintenance. The filter cost depends basically on the amount of components and materials used, for example the magnetic material for the core of inductors. FFT (Fast Fourier Transform) is developed using the digital oscilloscope. It is commonly used in digital signal processing to transform discrete time domain data to the frequency domain.

Fig.29 illustrates the different filters (L, LC and LCL) used in experimental test bench between the SEMIKUBE (inverter) and the DFIG's rotor.

5.1 Case 01: L-Type Filter

The L-Filter (fig.29-"1") is the first order filter with attenuation 20 dB/decade over the whole frequency range. To overcome the 3rd harmonic, LC-Filter is proposed (refer to Fig.29-"2") with same system-structure.

5.2 Case 02: LC-Type Filter

Fig.30 shows L-C output filter to obtain current and voltage equations.

By applying Kirchhoff's current law to nodes a, b, and c, respectively, the following voltage/current equations:

$$\begin{cases} \frac{dV_r}{dt} = \frac{1}{3*C_f} * I_f - \frac{1}{3*C_f} * I_r \\ \frac{dI_f}{dt} = -\frac{1}{L_f} * V_r + \frac{1}{L_f} * V_f \\ \frac{dI_r}{dt} = \frac{1}{L_r} * V_r - \frac{R_r}{L_r} * I_r \end{cases} . \quad (54)$$

Where: $\mathbf{V}_r = [V_{rab}\ V_{rbc}\ V_{rca}]^T$, $\mathbf{I}_f = [I_{fab}\ I_{fbc}\ I_{fca}]^T = [I_{fa}\text{-}I_{fb}\ I_{fb}\text{-}I_{fc}\ I_{fc}\text{-}I_{fa}]^T$, $\mathbf{V}_f = [V_{fab}\ V_{fbc}\ V_{fca}]^T$, $\mathbf{I}_r = [I_{rab}\ I_{rbc}\ I_{rca}]^T = [I_{ra}\text{-}I_{rb}\ I_{rb}\text{-}I_{rc}\ I_{rc}\text{-}I_{ra}]^T$.

The given plant model can be expressed as the following continuous-time state space equation:

$$\dot{x}(t) = A.x(t) + B.u(t) \quad (55)$$

Where:

$$x = \begin{bmatrix} V_r \\ I_f \\ I_r \end{bmatrix}_{9*1} \qquad A = \begin{bmatrix} 0_{3*3} & \frac{1}{3.C_f}.I_{3*3} & -\frac{1}{3.C_f}.I_{3*3} \\ -\frac{1}{L_f}.I_{3*3} & 0_{3*3} & 0_{3*3} \\ \frac{1}{L_{rotor}}.I_{3*3} & 0_{3*3} & -\frac{R_{rotor}}{L_{rotor}}.I_{3*3} \end{bmatrix}_{9*9} \qquad B = \begin{bmatrix} 0_{3*3} \\ \frac{1}{L_f}.I_{3*3} \\ 0_{3*3} \end{bmatrix}_{9*3} , u = [V_f]_{3*1}$$

5.3 Case 03: LCL-Type Filter

When compared with the previous topology, the LCL-filter (Fig.29-"3") has the advantage of providing a better decoupling between filter and DFIG impedance (reducing the dependence on DFIG parameters) and a lower ripple current stress across the grid inductor (since the current ripple is reduced by the capacitor, the impedance at the rotor side suffers less stress when compared with the LC topology). Like the LC-filter, increasing the capacitor value reduces filter cost and weight but with similar drawbacks. The split factor between the inductances at the inverter and grid side offers a further design flexibility.

The attenuation of the LCL-Filter is 60 (dB/decade) for frequencies above resonant frequency, there-fore lower switching frequency for the converter can be used. Knowing that in this case the values of inductance and capacitance are: L_1= 10 (mH), C= 66.56 (µF) and L_2= 1 (mH). Fig.31 demonstrates in details the differents element/paramter and values of the LCL filter (connected between the SEMIKUBE and the Rotor of DFIG). **[30]**

Following are a few important criteria for designing the LCL filter:

- Fulfillment of reactive volt-ampere reactive (VAR) limits (power factor nearly equals to 1).
- Optimal volume and weight with resulting minimum cost of passive (inductive and capacitive) components
- Attenuation of higher order harmonics from the output current (THD≤ 3%).
- Proper choice of resonance frequency such that the switching harmonics are sufficiently attenuated and the size of the filter components is not too large.

Transfer functions are the ratios between various inputs to output Laplace-transformed complex currents and voltages. The most pertinent transfer function for this LCL filter

(knowing that the LCL components/parameters and values are described in Table.3) is from the inverter voltage to the rotor current that is injected and is given by:

$$H_{LCL}(S) = \frac{I_{rotor}(s)}{V_{inv}(s)} = \frac{C.R_D.s + 1}{D_{LCL}} \tag{56}$$

Where:

$$D_{LCL} = C.L_1.L_2.s^3 + (C.L_1.R_2 + C.L_2.R_1 + C.L_1.R_D + C.L_2.R_D).s^2 + (L_1.L_2 + C.R_1.R_2 + C.R_1.R_D + C.R_2.R_D).s + (R_1.R_2) \tag{57}$$

Obtained using the equation:

$$H_{LCL}(s) = C.(s.I - A)^{-1}.B + D \tag{58}$$

Where A, B, C and D are matrices.

Fig.31-(b) describes the topology of an *LCL* filter. $V_{inv}(V)$ and $V_{Rotor}(V)$ are the inverter voltage (input) and grid voltage, respectively. Similarly, $I_{inv}(A)$, $I_c(A)$ and $I_{Rotor}(A)$ are the inverter, capacitor and the grid currents, respectively. Applying Kirchhoff's voltage and current laws to Fig.31-(b), we obtain the following:

$$I_{Inv} - I_{Rotor} = I_C \tag{59}$$

$$I_C = C * \frac{dV_c}{dt} \tag{60}$$

$$V_{L1} = L_1 * \frac{dI_{Inv}}{dt} = V_{Inv} - R_1.I_{Inv} - V_C - R_D.I_C \tag{61}$$

$$V_{L2} = L_2 * \frac{dI_{Rotor}}{dt} = V_C - V_{Rotor} + R_D.I_C - R_2.I_{Rotor} \tag{62}$$

Rearranging these, we get:

$$\frac{dI_{Inv}}{dt} = \frac{1}{L_1}.[-(R_1 + R_D)I_{Inv} + R_D.I_{Rotor} - V_C + V_{Inv}] \tag{63}$$

$$\frac{dI_{Rotor}}{dt} = \frac{1}{L_2}.[R_D.I_{Inv} - (R_2 + R_D).I_{Rotor} + V_C - V_{Rotor}] \tag{64}$$

$$\frac{dV_c}{dt} = \frac{1}{C}.[I_{Inv} - I_{Rotor}] \tag{65}$$

The representation of eqs: ((62), (63) and (64)) in state space form is:

$$\begin{pmatrix} \frac{dI_{Inv}}{dt} \\ \frac{d.I_{Rotor}}{dt} \\ \frac{dV_c}{dt} \end{pmatrix} = \begin{pmatrix} -\frac{(R_1 + R_{Inv})}{L_1} & \frac{R_D}{L_1} & -\frac{1}{L_1} \\ \frac{R_D}{L_2} & -\frac{(R_2 + R_D)}{L_2} & \frac{1}{L_2} \\ \frac{1}{C} & -\frac{1}{C} & 0 \end{pmatrix} . \begin{pmatrix} I_{Inv} \\ I_{Rotor} \\ V_c \end{pmatrix} + \begin{pmatrix} \frac{1}{L_1} & 0 \\ 0 & -\frac{1}{L_2} \\ 0 & 0 \end{pmatrix} . \begin{pmatrix} V_{Inv} \\ V_{Rotor} \end{pmatrix} \tag{66}$$

We define the state vector as:

$$x = \begin{pmatrix} I_{Inv} \\ I_{Rotor} \\ V_c \end{pmatrix} \tag{67}$$

And the input vector as:

$$u = \begin{pmatrix} V_{Inv} \\ V_{Rotor} \end{pmatrix} \tag{68}$$

The output (Y) equation:

$$Y = I_{Rotor} = (0).I_{Inv} + (1).I_{Rotor} + (0).V_C + (0).V_{Inv} + (0).V_{Rotor} \tag{69}$$

The state space representation of this equation is:

$$Y = \begin{pmatrix} 0 & 1 & 0 \end{pmatrix} . \begin{pmatrix} I_{Inv} \\ I_{rotor} \\ V_C \end{pmatrix} + \begin{pmatrix} 0 & 0 \end{pmatrix} . \begin{pmatrix} V_{Inv} \\ V_{Rotor} \end{pmatrix} \tag{70}$$

Now, we write the complete state space form of the LCL filter model (eqs. (66) and (70) as:

$$\begin{cases} \dot{x} = A.x + B.u \\ y = C.x + D.u \end{cases} \tag{71}$$

Where the matrices A, B, C and D are defined as:

$$A = \begin{pmatrix} -\frac{(R_1+R_{Inv})}{L_1} & \frac{R_D}{L_1} & -\frac{1}{L_1} \\ \frac{R_D}{L_2} & -\frac{(R_2+R_D)}{L_2} & \frac{1}{L_2} \\ \frac{1}{C} & -\frac{1}{C} & 0 \end{pmatrix}. \quad (72)$$

$$B = \begin{pmatrix} \frac{1}{L_1} & 0 \\ 0 & -\frac{1}{L_2} \\ 0 & 0 \end{pmatrix}. \quad (73)$$

$$C = (1 \quad 0 \quad 1) \quad (74)$$

$$D = (0 \quad 0) \quad (75)$$

Neglecting all the three resistances (in order to simplify the transfer function), eq. (56) reduces **[63]**:

$$H_{LCL}(S) = \frac{1}{C.L_1.L_2.s^3 + (L_1 + L_2).s} \quad (76)$$

5.4 Design and application of Bode plot in the three filters' transfer function.

The above transfer functions (TF) are expressed in terms of magnitude and angle phase margins (Bode plot). Table.4 illustrates the different type-filter studied in this section using Bode plot for both loads: resistive and inductive load. LCL-type filter with damp is basically the same LCL-filter plus the serial damping resistor R_D (Ω); the main aim of this latter is provide damp magnitude for the high frequency and to ensure the stability of the power system for response frequency.

Fig.32-(case 01 and case 02) depict the Bode plot of four (04) type-filter under tow load cases (resistive and inductive load). It can be seen that the magnitude of four type-filter (L, LC, LCL without damp and LCL with damp) have heroically the same characteristic in low frequency except the LCL-filter without damp (3rd order transfer function in the case of inductive); the remarkable peak magnitude is noted. On the other hand, LCL-Type filter with damp provide the magnitude in high frequency in construct of the without damp one. The damp phenomena is made by the mean of the damp resistor R_D which is placed in serial with the Capacitance (refer to Fig.31-b). In generally, the attenuation of the LCL-Filter is - 60 (dB/decade) for frequencies above resonant frequency, there-fore lower switching frequency for the converter can be used. The resonance frequency should be included in a range between 10 times the line frequency and 1/2 of the switching frequency in order not to generate resonance problems in the higher and lower parts of the harmonic spectrum **[34]**. Moreover, the damping of the LCL filter has a better performance compared to the L and LC filters above the switching frequency as expected.

5.5 Experimental results of Vs and Vr for three Types-Filter (L, LC & LCL) using FFT strategy

5.5.1 Experimental results of case 01 (L-type Filter)

Therefore the application of this filter type is suitable for converters with high switching frequency, where the attenuation is sufficient. On the other side inductance greatly de creases dynamics of the whole system converter-filter. In this case L= 10 (mH).

Figs.33-(1, 2, 3, 4, 5, 6, 7 and 8) illustrate the experimental results of rotor' and stator voltages (V_r and V_s) waveforms respectively of whole system: inverter (DC/AC) + Filter (L) + DFIG (Rotor); in transient and steady states under four (04) cases in term of current variation (I_{rd}* and I_{rq}*) as described in Table.5.

It is clear that the waveforms of Vr and Vs have taken the same inverter's waveforms in the case of only RL-load, with magnitude equals to 77 V and 90 V respectively for V_r and V_s, means that the L-filter can't provide the sinusoidal voltage waveforms under currents variation. In this test, it can be seen that the Ird and Irq had big impact on rotor/stator voltage waveforms as demonstrates the follows Figs.33-(2, 4, 6 and 8). The higher the current value the narrower the shape of the voltage pattern as Fig.33-(8).

Fig.34-(L-type Filter) demonstrates the experimental results of rotor' and stator' voltages (V_r and V_s) waveforms respectively of whole system and theirs Fast Fourier Transform (FFT) via L-Filter in transient and steady states under the first case (same as the Figs.34-(1, 2, 3 and 4)) in term of current variation as follows:

- FFT Study case: I_{rd}*= 0(A) and I_{rq}*= 0(A); (refer to Figs.34-(1 and 2) illustrates the rotor waveform and it's FFT and Figs.34-(3 and 4) illustrates the stator waveform and its FFT with
  magnitude equals to 77 (V) for V_r and 90 (V) for V_s.
- It can be seen that the FFT demonstrates different impairs harmonics, in Figs.34-(1 and 2) the FFT of rotor voltage (V_r) show that the 3rd hamonic equals to 250 (Hz), means the fundamental voltage signal is affected by the ripples, and it is necessary to remove/or overcome this power quality drawback.
- In Figs.34-(3 and 4) the FFT of stator voltage (V_s) show that the 3rd hamonic equals also to 250 (Hz), means the fundamental voltage signal is affected by the undulations/ ripples, and it is necessary to remove/or overcome this power quality disadvantage.

5.5.2 Experimental results of case 02 (LC-type Filter)

The own design of the LC-Filter is a compromise between the value of the capacity and inductance. The high capacity has positive effects on the voltage quality. On the other hand higher inductance value is required to achieve demanded cut-off frequency of the filter. Connecting system with this kind of filter to the supply grid, the resonant frequency of the filter becomes dependent on the grid impedance and therefore this filter is not suitable, too.

Fig.34-(LC-type Filter) demonstrates the experimental results of rotor' and stator' voltages (V_r and V_s) waveforms respectively of whole system and theirs Fast Fourier Transform (FFT)

via LC-Filter in transient and steady states keeping d-q axis components rotor current constant (I_{rd}* and I_{rq}*) as follows

- FFT Study case: I_{rd}*= 0(A) and I_{rq}*= 0(A); Figs.34-(5 and 6) depict the rotor voltage waveform and it's FFT, and Figs.34-(7 and 8) illustrate the stator voltage waveform and it's FFT with magnitude equals to 77 (V) for V_r and 90 (V) for V_s.

It can be seen that the FFT demonstrates the different impairs harmonics, in Figs.34-(5 and 6) the FFT of rotor voltage (V_r) show that the 5th hamonic equals to 250 (Hz), means the fundamental voltage signal is less affected by the ripples, contrary to FFT of rotor and stator voltage using L-Type Filter (Fig.29-1).

In Figs.34-(7 and 8) illustrate the FFT of stator voltage (V_s) show that the 5th hamonic equals also to 250 (Hz), means the fundamental voltage signal is less affected by the undulations/ ripples, and it is necessary to remove/or overcome this power quality drawback, contrary to FFT of rotor' and stator' voltage using L-Filter.

It is clear that the waveforms of rotor' and stator voltages (V_r and V_s) have taken the same inverter's waveforms in the case of only RL-load. To solve this problem, 3rd order Type-Filter is proposed called LCL-Filter; to keep the sinusoidal waveforms of the stator' and rotor voltages with neglected harmonics (the main objective of this paper).

5.5.3 Experimental results of case 03 (LCL-type Filter)

Fig.34-(LCL-Type Filter) demonstrates the experimental results of rotor' and stator voltages (V_r and V_s) waveforms respectively of whole system and theirs Fast Fourier Transform (FFT) via LCL-Filter in transient and steady states by keeping d-q axis components rotor current constant (I_{rd}* and
and I_{rq}*) as follows:

- FFT Study case: I_{rd}*= 0(A) and I_{rq}*= 0 (A); (refer to Figs.34-(9 and 10) illustrate the rotor voltage waveform and it's FFT and Figs.34-(11 and 12) illustrate the stator voltage waveform and its FFT with magnitude equals to 77 (V) for V_r and 90 (V) for V_s.
- It can be seen that the FFT demonstrates the different impairs harmonics, in Figs.34-(9 & 10) the FFT of rotor voltage (V_r) show that the 7th hamonic equals to 250 (Hz), means the fundamental voltage signal is not affected by the ripples, contrarily the FFT of rotor and stator voltage using LC-Filter (Figs.34-6 and 8)).
- In Figs.34-(11 & 12) the FFT of stator voltage (V_s) show that the 7th hamonic equals also to 250 (Hz), means the fundamental voltage signal is not affected by the undulations/ ripples. In Figs.34-(12) it can be seen an excellent sinusoidal waveforms in steady and transient states.
- For these reasons LCL-type filter is keeping for all the next experimental tests validation.

5.6 Overview recapitulation of experimental studies (L, LC & LCL Filters)

After had been explained the above experimental study, it can be summarized the impact of the filter choice on the current/power quality, Table.6 demonstrates in details the performances according to each filter type.

6. Simulation and experimental results

6.1 Simulation results

The proposed system (DFIG control + wind turbine) is validated using Matlab/Simulink® software under MPPT strategy by keeping stator reactive power equals to zero and to ensure unity power factor (PF=1). The full simulation conditions are described in Appendix section (Table.26).

The Figs.35-(Mode 1, 2 & 3) respectively present the simulation results of proposed power control, in this case the wind-system based on DFIG 4 kW and Wind Turbine 4.5 kW (please refer to Appendix section; Tables-(20 & 21) respectively).

1- The first part depicts the behavior of the wind-system parameters under three (03) modes -*knowing that for each mode we present the differents proposed topologies*- as follows:Fig.35 shows the behavior of wind-system parameters under three proposed Modes:

- **Mode 1**-(red color/ Fig.35): Without MPPT Strategy, in this case we impose the Ps and Qs reference profiles, Max wind speed = 11.75 m/s (refer to the Table.7)
- **Mode 2**-(blue color/ Fig.35): With MPPT strategy, in this case we propose a low wind speed based on step form (Max wind speed = 11.5 m/s) by keeping stator reactive power equal to Zero level “Qs = 0 (Var)”; to ensure only the exchange of the stator active power to the RL-load; means following the maximum active power point.
- **Mode 3**-(green color/ Fig.35): With MPPT strategy, in this case we propose a medium wind speed based on random form (Max wind speed = 13.5 m/s) by keeping stator reactive power equal to Zero level “Qs = 0 Var”; to ensure only the exchange of the stator active power to the RL-load; means following the maximum active power point.

2- The second part shows the DFIG operations modes by the mean of the sinusoidal rotor currents variation

3- The third part illustrates the behavior of grid voltage and stator current and the power-flow for three (03) proposed modes.

4- The fourth part shows the decoupling terms "d-q axis" test (using novel reference powers profile)

5- The fifth part presents the robustness tests of the wind-system conventional and proposed control
under three (03) proposed modes.

6.1.1 Wind-system parameters based on three (03) mode

The electrical parameters are defined (the same order applied for all modes; from “a” to “i”) as follows:

The measured stator active and reactive powers (P_{s_meas} and Q_{s_meas}) and their references (P_{s_ref} and Q_{s_ref}) profiles are presented together in Figs.35-(a) and are presented separately in Figs.35.(b and c) respectively. The reference stator active and reactive powers are indicated in Table.7. The direct and quadrature components of currents and flux (I_{rd}, I_{rq} and Φ_{rd}, Φ_{rq}) are presented respectively in Figs.35
-(e and g), which present the inverse diagrams compared to reactive and active powers. The inverse case for stator direct and quadrature currents (I_{sd}, I_{sq}) which have the same graphs of reactive and active powers, and they are presented in Figs.35-(d). The power error is presented in Figs.35-(f). The stator’ and rotor currents; I_{s_abc} and I_{r_abc} are shown in Figs.35-(h and i) respectively, we remark the sinusoidal form of the three rotor and stator phases currents, have a good THD of stator currents (<= 5 % respect the IEEE-519 Std). The zooms of Figs.35-(b & c) depict the fast dynamic, neglected overshoot, small static error and excellent tracking reference powers for all modes. The zooms of Figs.35-(i) help us to define easily the sub and super-synchronous operations by the sense variation of rotor currents (I_{rabc}).

It is noted also that only sub synchronous operation is applied in Mode-(01 and 02), but in Mode-03 it can be seen that both sub and super-synchronous operations are applied; which means that the rotor could absorb and inject the power ($Pr=S*P_n$) respectively from/to the grid. In order to ensure the high performances; the DFIG should operate in stable zone (as shown in Fig.37) means that the slip should be in this interval ($-0.3<S<+0.3$).

Table.8 depicts the recapitulation results of the proposed control performance in three modes; such as: Stator current THD (%), overshoot (%), response time (s) and finally power error (+/- W_Var).

6.1.2 Power Factor (PF) tests for three (03) modes

Fig.36 presents the relationship between the sign of electromagnetic torque, slip, rotor speed and the power-flow in/out of stator and rotor. In this paper, only the generator operation modes are studied.

Fig.37 depicts the relationship *Torque/Speed* characteristic of *DFIM* in four (04) quadrants under both modes: *Motoring and Generating.*

It should be noted that for Sub- and Super-synchronous generating modes, the power flows through the rotor are of opposite directions (refer to Figs.38-(d)).

The electrical parameters are defined (the same order is adopted for all modes; from “a” to “f”) as follows:

In Figs.38-(a) the generator speed (rpm) basically took the wind speed form; is constant (≈ 1441 rpm) for Mode-01, is variable and inferior than 1500 (rpm) for Mode-02; is variable “inferior /superior” respectively than 1500 (rpm) for Mode-03. Figs.38-(b) repesent the slip, which equals to speed ratio ($S= (\omega_s-\omega)/\omega_s = (N_s-N)/Ns$), presents only the positive values for Mode-01 and Mode-02; “because the rotation speed was always inferior than the synchronous speed”, and presents the postive/negative values “because some time the rotation speed was inferior/superior than the synchronous speed”. Figs.38-(c) repesent the stator power (P_s (W)) which are already discussed in previous section. Figs.38-(d) repesent the rotor power, it can be seen that the P_r (W) took positive value mean the rotor absorbe the power in Mode-01 and Mode-02; in this case the DFIG operateonly in Sub-synchronous mode and only the stator inject the power to the Load. For the Mode-03, the Pr (W) took positive/negative; in the case of positive value mean that the rotor speed is inferior than the synchronous speed ⇒ the slip is postive ⇒ the sub-synchronous operation is applied⇒ the rotor absorbe the power from the grid via the Back-to-Back converter (maximum 30% from the rated power, in order to limit the DFIG operation in the stable zone; refer to Fig.37).

And in the case P_r (W) took negative value; mean that the rotor speed is superior than the synchronous speed⇒the slip is negative⇒the Super-synchronous is applied⇒ the rotor inject the power to the grid via the Back-to-Back converter (knowing that; the sizing of the converters is quite important, because if an error occurs the damage will be catastrophic especailly in Experimental tests).

Figs.38-(e) display the power factor (PF), it is clear that the PF depends on the reactive power variation ($PF = Ps/S = Ps/\sqrt{(Ps^2 + Qs^2)}$); if Q_s is near than zero (0 Var)), mean that the PF is near the unity. In Mode-01 the PF took the unity because the reactive power (Q_s (Var)) takes the zero level means the PF maintain the unity in the interval: 0→0.2(sec), 0.4→0.6(sec), 0.8→1(sec) and 1.2→1.4(sec)) which equals PF=0.995, otherwise the PF dosen’t maintain the unity factor in the interval: 0.2→0.4(sec), 0.6→0.8(sec), 1→1.2(sec) and 1.4→1.5(sec); due to the superior reactive power value; in this case the PF inferior than 0.7. For Mode-02 and Mode-03 the PF took the unity value because the MPPT strategy keep stator reactive power equal to zero level “Qs = 0 (Var)”; to ensure only the exchange of the stator active power to the RL-load; which PF=0.998.

Figs.38-(f) present the behavior of the pahse grid voltage (V_{ga}) and stator currents (I_{sa}) under stator powers variation. It is remarkable that the angle between stator current and gird voltage θ_{Isa_Vga} equals to 180° for the three modes; which explains that the DFIG operate as generator in this case and generate the active power to RL-load. Knowing that; in Mode-01

the stator current equals to: (I_{sa}=25*I_{real}), for Mode-02 the stator currents equals to (I_{sa}=15*I_{real}) and for Mode-03 the stator current equals to (I_{sa}=10*I_{real}).

6.1.3 The DFIG operations modes:

In this test; the following numerotation is adopted such as;

The " **zone 01** " ⇒ presents Sub-synchronous operation, and " **zone 02** " ⇒ illustrates the Super-synchronous operation.

In this section, DFIG operation modes are illustrated by the mean of the sinusoidal rotor currents variation. Fig.39 illustrates the behavior of rotor measured current when the speed varies near than 1500 rpm (Synchronous speed). Both cases are studied; from sub-synchronous to super-synchronous and the inverse.

It can be seen that the rotor currents took the same form the wind speed (random wind speed in this case); because I_{r_abc} (A) were been controlled using the angle slip $\boldsymbol{\theta}_{slip}$ $=\int_0^t(\omega_{slip} = \omega_s - \omega_r)\, dt + \theta_{s0}$ and ω_s=2π*f; ω_r =P* Ω_{mec}) and this later based on DFIG rotor-speed which mean Wind speed (extracted from the MPPT strategy); knowing that the rotor current in this case were multiplied by 80 (⇒I_{rabc}*80). So the rotor power-flow is explained by the rotor current changement sense; from

Sub-to-Super ⇒ the rotor absorb and from Super-to-Sub⇒ the rotor inject the power into the grid via B-2-B converter. Table.9 depicts the value of DFIG speed under both studied cases.

6.1.4 The Decoupling terms "d-q axis" test:

In this section, a comparative study (refer to Figs.40-(case 01 and case 02)) is presented to show the decoupling terms (under d and q axes) using the proposed and conventional algorithms in this paper.

The main aim of this simulation study is to show the high performance offered by the improved DPC compared to conventional DPC power control in terms of decoupling d-q axis components, neglected power error and high tracking power. Knowing that in this tests, a novel reference power profiles are proposed in order to show clearly the coupling terms between active and reactive power in each case (refer to Table.10).

Figs.40-(case 01 and case 02) illustrate the behavior of stator measured active and reactive powers and theirs references respectively; in transient and steady states. The coupled terms between d-q axis component of each case (conventional and proposed respectively) is explained by red circle which is very small in proposed one.

6.1.5 Robustness tests:

Figs.41-(Mode 01, Mode 02 & Mode 03) illustrate the behavior of stator measured active and reactive powers and theirs references respectively under parameters variations; knowing that the vari-

-ation made in the robustness tests is illustrated in Table.11.

A- Mode I (conventional and proposed DPC/imposed power references):

In Figs.41-(Mode-01), it can be noted big power error in conventional control with remarkable undulations especially in transient and steady states compared to propose one.

The value of power error reaches nearly ±1000 (W_Var) for conventional and near than +/-200 W_Var for proposed one. A remarkable overshoot is noted in conventional control especially at: 0.4, 0.8, and 1.2(sec) which present more +120% and near than 18% for proposed one.

B- Mode II (conventional and proposed DPC/MPPT based on step wind speed):

Figs.41-(Mode-02) display the behavior of stator active and reactive powers under MPPT strategy by maintaining the reactive power equals to zero value. In this case the active power had taken the inverse step profile of wind speed. Using robustness tests a remarkable undulations are noted especially at 0.6 (sec) which presents the rated power of DFIG (P=4 KW)). On other hand and in the same time a remarkable power error is noted in stator reactive power for the conventional control (which means the PI controller can't maintain the unity power factor "PF=1" under maximum wind power and parameters variation). Also a very big overshoot is noted in steady state (in measured stator powers P_{s_meas} & Q_{s_meas}) of the conventional control.

C- Mode III (conventional and proposed DPC/MPPT based on random wind speed):

Figs.41-(Mode-03) display the behavior of stator active and reactive powers under MPPT strategy by maintaining the reactive power equals to zero value. In this case the active power had taken the inverse random profile of wind speed. Using robustness tests a remarkable undulations are noted in conventional control especially at 0.75 (sec) and 0.8 (sec) which presents the over rated power of DFIG (P=4 (kW) and the measured active power maintain 4.6 (kW)), with very bad tracking.

On other side a remarkable power error is noted in stator reactive power for conventional control (which means that the PI controllers can't maintain the unity power factor under maximum wind power), also a very high overshoot is noted in transient and steady states of active and reactive power.

6.2 Brief comparative study based on latest control schemes

According to the Table.12, it is obvious that the proposed control offers high dynamic performances in transient and steady states. For the rest of the criteria which are mentioned with (-); unfortunately, they are not available in the references.

Knowing that:

NNC: neural network Controller, **SMC:** Sliding mode Controller, **HOSMC:** High order sliding mode controller, **STSMC**: Super Twisting Sliding Mode Control, **BSC:** Backstepping controller, **DPC:** Direct power control, **PDPC**: Predictive Direct Power Control, **DTC:** Direct Torque Control, **HC**: Hysteresis Controller, **PI-R**: regulator PI resonant, **PI-V**: variable PI, **MDPC**: Model Direct Power Control, **VC:** Vector Control, **FLC**: Fuzzy Logic Control, ISM:

Integral Sliding Mode. **FOSMC**: Fractional Order Sliding Mode Control, **NSMC:** Neural Sliding Mode Control, **ASMT-2NFC**: Adaptive Sliding Mode Type-2 Neuro-Fuzzy Controller.

6.3 Experimental results

The experimental tests on a 4.5 KW-scaled laboratory setup are carried out to validate the effectiveness of the proposed control strategy. The parameters and configurations (DFIG is 4.5 KW and Wind-turbine is 4 KW) are given in Appendix section (Tables-(22 and 23)) respectively.

The following experimental results are giving under in three (03) operations zone (sub-synchronous, Synchronous & Super-synchronous zone) using dSPACE1103 card, ControlDesk and Matlab/Simulink® environment.

In order to ensure the robustness and feasibility of the proposed control system; four (04) experimental tests are made with many reference variation as demonstrate in Table. 13.

6.3.1 Test 01: Rotor currents variation

Case I: d-q axis rotor currents components (under trapezoid form):

Fig.42-(a) depicts experimental results of rotor direct and quadrature currents (I_{rd} (A) and I_{irq} (A)) variation using trapezoid form in transient and steady states (in the period of 40 (sec)). It can be seen that the rotor direct and quadrature measured currents (I_{rd_meas} (A) and I_{rq_meas} (A)) follow exately their

references (I_{rd}*(A) and I_{rq}*(A)) respectively despite the sudden variation of the I_{rd}*(A) and I_{rq}*(A).

Figs.42-(a-1 & a-2) illustrate the zoom points (1 and 2) of rotor current behavior in steady state, it can be seen that the overshoot is neglected (between +0.5% and +2 %), a perfect decoupled control between d-q axis currents components is noted despite currents reference variation. the response time is very short, perfect current tracking and low current error. Table.14 recapitulates all the performance criteria of rotor currents variation (I_{rdq} (A) sung trapezoid form: variation values, overshoot (%), response time (msec), current error and tracking reference.

Case II: d-q axis rotor currents components (under step form):

Fig.43-(b) shows the experimental results of rotor direct and quadrature currents (I_{rd} (A) and I_{rq} (A)) variation using step form in transient and steady states (in the period of 40 (sec)). It can be seen that the rotor direct and quadrature measured currents (I_{rd_meas} (A) and I_{rq_meas} (A)) follow exately their references (I_{rd}*(A) & I_{rq}*(A)) respectively regardless I_{rd}*(A) & I_{rq}*(A) sudden variation. Figs.43-(b-1 & b-2) illustrate the zoom points (1 and 2) of rotor current behavior in steady state, it can be seen that that the overshoot is acceptable (few/between +7%, 8% and 12 %), a good decoupled control between d-q axis currents components is noted regardless of currents reference variation, response time is very short < 35 (msec), good tracking currents and neglected current error are noted.

Table.14 summaries all the performance criteria of rotor currents variation (I_{rdq} (A) sung trapezoid form: variation values, overshoot (%), response time (msec), current error (A) and tracking reference.

6.3.2 Test 02: Sensevity to the wind speed variation

In this section, a brief demonstration of slip angle (θ_{slip} (rad)) and rotor current I_{ra_meas} (A) behavior when the rotor speed Ω_r (rad/sec) variation is made.

Figs.44-(a and b) illustrates sinusoidal waveform of rotor current variation and the slip angle value. It can be seen that the variation of I_{ra_meas} (A) has no effect because the angle slip value is theoretically based on rotor angle and grid angle (knowing that in this case the rotor angle equals to zero; means that the slip angle equal directly to grid angle ($\theta_{slip} = \theta_{grid} - \theta_{rotor} = \theta_{grid} - 0 = \theta_{grid}$ (rad)) because the rotor speed Ω_r (rad/sec) $=N_{r10}$ (rpm) = 0 (rpm) $\Rightarrow$ Generator stopped.

Figs.44-(c and d) depicts present the behavior of the rotor measured current waveform in transient and steady states in the same time of the rotor speed variation N_r (rpm). It can be seen the sense
changement of rotor current when the rotor frequency equals to stator frequency (which means the slip equals to zero), in this point the rotor injected the power in to the grid, and this operation zone called “Super synchronous zone” because both the rotor and stator inject the power into the grid. Table.15 recapitulates the different variation and the periods made in this section (a detail values).

6.3.3 Test 03: Sub and Super-synchronous operation mode under fixed wind speed:

In this test, the rotor speed is kept constant for each operation mode, and the d-q axis components are variable. The main objective of this test is to show the behavior of the DFIG-Wind turbine system
in transient and steady states for three operation mode.

Figs.45-(a, 1, 2: Sub synchronous Mode; N=1000 rpm) shows the experimental results of the behavior of measured rotor and stator currents waveforms (I_{ra_meas}(A) and I_{sa_meas}(A)) under direct and quadrature currents (I_{rd}*(A) and I_{rq}*(A)) using Step form in transient and steady states in the period of 40 (sec) = (40 (sec) *10); “Knowing that in this case the stator is connected into the RL-load”. The variation of rotor current in this case is adopted as mentioned in Table.16.

Figs.45-(b, 1, 2: Synchronous Mode; 1500 rpm) shows the behavior of measured rotor and stator currents (I_{ra_meas} (A) and I_{sa_meas} (A)) waveforms under direct and quadrature currents using Step form in transient and steady states in the period of 40 (sec).

The variation of rotor current in this case is adopted as mentioned in Table.16.

Figs.45-(c, 1, 2: Super-synchronous mode) shows the experimental results of the behavior of measured rotor and stator currents (I_{ra_meas}(A) and I_{sa_meas}(A)) waveforms under direct and quadrature currents (I_{rd}*(A) and I_{rq}*(A)) variation using Step form in transient and steady states in the period of 40 (sec).The variation of rotor current in this case is adopted as mentioned in Table.16. Period, waveform quality, rotor frequency and rotor peak for two points ("zoom 1 & zoom 2" from Fig.45-a-b-c respectively) are explained in details in Table.17.

6.3.4 Test 04: Power quality improvement

In this test, the rotor speed is kept constant, and the d-q axis components are also constant. Fig.46-(1) shows perfect sinusoidal waveforms of stator and rotor voltages. An improvement power quality (based on sinusoidal waveforms and THD_v: voltage total harmonic distortion <5% for stator voltage) is noted which respect the IEEE 519^{std}. With the same manner for stator current injected into the RL-load, which had sinusoidal form (Fig.46-2) in differents operation speed and the stator current $THD_i \approx 1.5$ %.

6.4 Detail recapitulation of experimental studies power control Wind-Turbine under: Grid-connection and Stand-alone mode respectively

After had being explained the experimental results under differents tests, a recapitulation review have been proposed of power control in WECS in both mode: Grid connection mode and Stand-alone mode. Tables-(18 and 19) present brief review of power control in Grid-connection and Stand-alone modes respectively (which based only on experimental studies). Many criteria were been taken into account in order to show the advantage/disadvantages of each control strategy. For the rest of the numerical values of the performance which are mentioned with (/); unfortunately, they are not available in the references.

7. Conclusion

In this paper, a new stand-alone DPC of DFIG has been suggested and experimented in real time (RTI). IP controllers have been applied in place of conventional "PI" controllers to control Ird and Irq (images of Qs and Ps respectively). In fact, the stability study of the Transfer Function shows the superiority of the IP controller especially when the rotor currents/wind speed change. The filter settings and resonance phenomena must be carefully designed to overcome possible stresses and oscillations. In order to enhance the power quality which will be injected to the RL load, the LCL passive filter is selected as the most suitable filter in terms of THD of the injected current, it is implemented between the rotor of the DFIG and the DC-AC converter in such a way to improve the quality of the current and voltage delivered to the stator. In addition, this approach achieved a unity power factor grid operation (≈ 0.98).

Various simulation and experiments tests have been established to show the behavior of

the proposed wind system in both transient and steady states, and also to ensure that the proposed control is able to operate under a variety of wind speed conditions (three operating modes). At last, the experimental results have proved the high performance of the proposed control in terms of response time, overshoot, current and power errors.

- For future work that depends on the same DFIG-wind turbine design:

- A comparative experimental study of existing "power/current" controls will be an excellent proposed research work; to overcome the drawbacks of conventional control algorithms and show the improvement of the proposed one.
- The design and analysis of the network connected topology is an interesting experimental research work, especially in the case of the unbalanced network.
- The use of advanced controllers such as Backstepping controller and higher order sliding mode controllers are assumed to be an attractive alternative to the IP controller (the disadvantage of the IP: the gain values depend on the parameters of the wind power system).
- The use of optimization algorithms (such as PSO and genetic algorithms) to accurate identifies the gain values of the suggested controllers quickly.
- In order to enhance the power quality and output voltage, a back-to-back multilevel converter will be regarded as an appropriate alternative solution for the wind power system.
- Robustness tests that are based on the variation of electrical/mechanical parameters present the severe working conditions are the optimal tests to prove the adaptation of the power control algorithm. In this case, artificial intelligent controllers such as Fuzzy type 2 controllers (based on the three dimensions: X, Y and Z) and Neuro-Fuzzy controller present a good alternative solution and will be proposed to overcome this problem.

Acknowledgement:

We are very grateful to the Algerian Ministry of Higher Education and Scientific Research (MESRS) for funding this Research Project as part of an Algerian-French **PROFAS b+** Scholarship (collaboration research work between LAS-ALGERIA and L2EP-FRANCE laboratories). We are grateful for all L2EP laboratory team especially: Pr. Bruno FRANÇOIS, Mr. Xavier CIMETIERE and Simon THOMY (Full Professor, Engineer & Technician respectively at Central School Lille) for the help and good moments. We are grateful to Dr. SARI Billel for his precious guidance (LAS Laboratory, Setif-1 University).

Also, this research work falls within the framework of the research project "**PRFU**" under the code: A01L07UN400120190001 (Project approved from 01/01/2019).

8. References

[1] "FUTURE OF WIND: Deployment, investment, technology, grid integration and socio-economic aspects," International Renewable Energy Agency (IREA), 2019.

[2] A. P. FARROKH, N. HASHEMNIA, and A. KASHIHA, "Robust Speed Sensorless Control of Doubly-fed Induction Machine Based on Input-output Feedback Linearization Control Using a Sliding-mode Observer", World Applied Sciences Journal, vol: 10, no:11, pp.:1392-400, 2010.

[3] Y. SONG; F. BLAABJERG, "Overview of DFIG-Based Wind Power System Resonances Under Weak Networks", IEEE Transactions on Power Electronics, vol: 32, no: 6, pp: 4370 – 4394, 2017.

[4] D. ZHOU; F. BLAABJERG; T. FRANKE; M. TONNES and M. LAU, "Reduced Cost of Reactive Power in Doubly Fed Induction Generator Wind Turbine System with Optimized Grid Filter", IEEE Transactions on Power Electronics, vol: 30, no: 10, pp.: 5581 – 5590, 2015.

[5] A DJOUDI, S. BACHA, H. CHEKIREB, H. IMAN-EINI and C.BOUDINET, "Adaptive Sensorless SM-DPC of DFIG-Based WECS under Disturbed Grid: Study and Experimental Results", IEEE Transactions on Sustainable Energy, vol: XX, no: XX, DOI: 10.1109/TSTE.2017.2748966, 2017.

[6] G ABAD and G IWANSKI, "Properties and Control of a Doubly Fed Induction Machine", Power Electronics for Renewable Energy Systems, Transportation and Industrial Applications, First Edition, John Wiley & Sons, 2014.

[7] C. EVANGELISTA, F. VALENCIAGA and P. PULESTON. "Active and reactive power control for wind turbine based on a MIMO 2-sliding mode algorithm with variable gains" IEEE Transactions Energy Conversion, vol: 28, no: 3, pp.: 882-889, 2013.

[8] H. NIAN, Y. SONG, P. ZHOU and Y. HE. "Improved direct power control of a wind turbine driven doubly fed induction generator during transient grid voltage unbalance" IEEE Transactions Energy Conversion, vol: 26, no: 3, pp.: 976-986, 2011.

[9] F. BLAABJERG and K. MA, "Wind Energy Systems", proceeding of the IEEE, vol: 105, no: 11, 2017.

[10] D.SUN and X. WANG, "Sliding-mode DPC using SOGI for DFIG under unbalanced grid condition", IEEE Electronics Letters, vol: 53, no: 10, pp: 674–676, 2017.

[11] W. LEONHARD, "Control of Electrical Dives", 3rd ed. Berlin, Germany: Springer Verlag, 2003.

[12] R. DATTA and V. T. RANGANATHAN, "Direct power control of grid-connected wound rotor induction machine without rotor position sensors" IEEE Transactions on Power Electronics, vol: 16, no: 8, pp.: 390–399, May. 2001.

[13] V.-T. PHAN, D.-T. NGUYEN, Q.-N. TRINH, Cong-Long NGUYEN and Thillainathan LOGENTHIRAN, "Harmonics Rejection in Stand-Alone Doubly-Fed Induction Generators With Nonlinear Loads", IEEE Transactions on Energy Conversion, vol: 31, no:2, pp. 815-817, 2016.

[14] V. -T. PHAN and H. -H. LEE "Stationary frame control scheme for a stand-alone doubly fed induction generator system with effective harmonic voltages rejection", IET Electric Power Applications, vol: 5, no: 9, pp. 697-707, 2011.

[15] F. AMRANE, A. CHAIBA, B. FRANCOIS and B. BABES, "Experimental Design of Stand-alone Field Oriented Control for WECS in Variable Speed DFIG-based on Hysteresis Current Controller", IEEE 2017 15th International Conference on Electrical Machines, Drives and Power, Bulgaria, 2017.

[16] R. PENA, J. C. CLARE, and G. M. ASHER, "A doubly fed induction generator using back-to-back PWM converters supplying an isolated load from a variable speed wind turbine" IEE Proceeding. - Electronics Power Applications, vol. 143, no. 1, pp. 380–387, 1996.

[17] R. CARDENAS; Rubén PENA; S. ALEPUZ and G.ASHER, "Overview of Control Systems for the Operation of DFIGs in Wind Energy Applications", IEEE Transactions on Industrial Electronics, vol: 60, no: 7, pp.: 2776–2798, 2013.

[18] L. XU and P. CARTWRIGHT, "Direct Active and Reactive Power Control of DFIG for Wind Energy Generation", IEEE Transactions on Energy Conversion, vol. 21, no: 3, 2006.

[19] Y. ZHANG, J. HU and J. ZHU, "Three-Vectors-Based Predictive Direct Power Control of the Doubly Fed Induction Generator for Wind Energy Applications", IEEE Transactions on Power Electronics, vol: 29, no: 7, pp.: 3485-3500, 2014.

[20] H. MISRA, A.GUNDAVARAPU and A. K. JAIN, “Control Scheme for DC Voltage Regulation of Stand-Alone DFIG-DC System”, IEEE Transactions on Industrial Electronics, vol: 64, no: 4, pp.: 2700-2708, DOI: 10.1109/TIE.2016.2632066, 2017.

[21] G. D. MARQUES, and M. F. IACCHETTI, “Sensorless Frequency and Voltage Control in Stand-Alone DFIG-DC System”, IEEE Transactions on Industrial Electronics, vol: 64, no: 3, pp.: 1949-1957, DOI: 10.1109/ TIE.2016.2624262, 2017.

[22] H. MISRA and A. K. JAIN, “Analysis of Stand-Alone DFIG-DC System and DC Voltage Regulation With Reduced Sensors”, IEEE Transactions on Industrial Electronics, vol: 64, no: 6, pp.: 4402-4412, DOI: 10.1109/TIE.2017.2669889, 2017.

[23] F. BOUCHAFAA, D. BERIBER, and M. S. BOUCHERIT, “Modeling and control of a gird connected PV generation system,” in Control & Automation (MED), 18th Mediterranean Conference, pp.315 – 320, 2010.

[24] M. LISERRE, F. BLAABJERG, and S. HANSEN, “Design and Control of an LCL-Filter-Based Three-Phase Active Rectifier,” IEEE Transactions on Industry Applications, vol. 41, no. 5, pp. 1281–1291, Sep. 2005.

[25] J. GUERRERO, F. BLAABJERG, T. ZHELEV, K. HEMMES, E. MONMASSON, S. JEMEI, M. COMECH, R. GRANADINO, and J. FRAU, “Distributed generation: Toward a new energy paradigm,” IEEE Industrial on Electronics. Mag., vol. 4, no. 1, pp. 52 –64, march 2010.

[26] J. HE and Y. W. LI, “Hybrid voltage and current control approach for DG grid interfacing converters with LCL filters,” IEEE Transactions on Industrials Electronics, vol. 60, no. 5, pp. 1797–1809, 2013.

[27] T. GHENNAM, “Supervision d’une ferme éolienne pour son intégration dans la gestion d’un réseau électrique, Apports des convertisseurs multi niveaux au réglage des éoliennes à base de machine asynchrone à double alimentation,” PhD Thesis (in French language), 2011.

[28] H.VOLTOLINI, M. H. GRANZA, J.IVANQUI and R. CARLSON, “Modeling and Simulation of the Wind-Turbine Emulator using Induction Motor Driven by Torque Control Inverter“,10th IEEE Conference/IAS International Conference on Industry Applications, 2012.

[29] https://www.dspace.com/en/pub/home/products

[30] Y. TANG, P. C. LOH, P. WANG, F. H. CHOO, F. GAO, and F. BLAABJERG, “Generalized design of high performance shunt active power filter with output LCL filter,” IEEE Transactions on Industrial Electronics, vol. 59, no. 3, pp. 1443– 1452, 2012.

[31] F. AMRANE and A. CHAIBA. “Improved Indirect Power Control (IDPC) of Wind Energy Conversion Systems (WECS).” E-Book Bentham Science Publishers, pp.1-148, 2019.

[32] F.AMRANE, A. CHAIBA, B.E. BABES and S. MEKHILEF, “Design and Implementation of High Performance Field Oriented Control for Grid-Connected Doubly Fed Induction Generator via Hysteresis Rotor Current Controller”, Rev. Roum. Sci. Techn.– Électrotechn. et Énerg Vol: 61, n°: 4, pp. 319-324, 2016**.**

[33] V. PHAN and H. LEE, "Performance Enhancement of Stand-Alone DFIG Systems With Control of Rotor and Load Side Converters Using Resonant Controllers," in IEEE Transactions on Industry Applications, vol. 48, no. 1, pp. 199-210, Jan.-Feb. 2012.

[34] H. NIAN, and Y. SONG. “Direct Power Control of Doubly Fed Induction Generator Under Distorted Grid Voltage”. IEEE Transactions on Power Electronics, 29(2), 894–905, 2014.

[35] X. WANG and D. SUN, "Three-Vector-Based Low-Complexity Model Predictive Direct Power Control Strategy for Doubly Fed Induction Generators," in IEEE Transactions on Power Electronics, vol. 32, no. 1, pp. 773-782, Jan. 2017.

[36] Zhou, D., Wang, H., & Blaabjerg, F. “Reactive Power Impacts on LCL Filter Capacitor Lifetime and Reliability in DFIG Grid-Connected Inverter”, IEEE Energy Conversion Congress and Exposition (ECCE), 2018.

[37] S. NAIDU, N. K., & B. SINGH, “Doubly Fed Induction Generator for Wind Energy Conversion Systems with Integrated Active Filter Capabilities”. IEEE Transactions on Industrial Informatics, 11(4), 923–933, 2015.

[38] L. DJILALI, E. Sanchez, & M. BELKHEIRI, “Real-Time Neural Sliding Mode Field Oriented Control for a DFIG Based Wind Turbine under Balanced and Unbalanced Grid Conditions”. IET Renewable Power Generation, 2019.

[39] A, M. AMIN., & O. A. MOHAMMED, “Development of High-Performance Grid-Connected Wind Energy Conversion System for Optimum Utilization of Variable Speed Wind Turbines”, IEEE Transactions on Sustainable Energy, 2(3), 235–245, 2011.

[40] R. GALINDO DEL VALLE, M. COTOROGEA, B. RABELO, & W. HOFMANN, “On the Emulation of an Isolated Wind Energy Conversion System: Experimental Results”, Electronics, Robotics and Automotive Mechanics Conference (CERMA), 2009.

[41] E.G. SHEHATA and G. M. SALAMA, “Direct power control of DFIGs based wind energy generation systems under distorted grid voltage conditions”, Electrical Power and Energy Systems, vol. 53, pp. 956-966, 2013.

[42] M. V. KAZEMI, A. S. YAZDANKHAH and H. M. KOJABADI, “Direct power control of DFIG based on discrete space vector modulation” Renewable Energy, vol. 35, pp. 1033–1042, 2010.

[43] M. J. ZANDZADEH and A. VAHEDI, “Modeling and improvement of direct power control of DFIG under unbalanced grid voltage condition”, Electrical Power and Energy Systems, vol.59, pp. 58-65, 2014.

[44] F. MAZOUZ, S. BELKACEM, I. COLAK, S. DRID and Y.HARBOUCHE, “Adaptive direct power control for double fed induction generator used in wind turbine”, Electrical Power and Energy Systems, vol.114, pp. XX-XX, 2020.

[45] A. DIDA, F. MERAHI and S. MEKHILEF, “New grid synchronization and power control scheme of doubly-fed induction generator based wind turbine system using fuzzy logic control”, Computers and Electrical Engineering, vol.84, pp. xx-xx, 2020.

[46] K. BEDOUD, M. ALI-RACHEDI, T. BAHI, R. LAKEL and A. GRID, “Robust Control of Doubly Fed Induction Generator for Wind Turbine under Sub-Synchronous Operation Mode”, Energy Procedia, vol.74, pp. 886-899, 2015.

[47] I. K. AMIN, and M. NASIR UDDIN, “Nonlinear Control Operation of DFIG-Based WECS Incorporated With Machine Loss Reduction Scheme”, IEEE Transactions on Power Electronics, vol. 35, no. 7, pp. 7031-7044, 2020.

[48] V.-T. PHAN, and H.-H. LEE, “Control Strategy for Harmonic Elimination in Stand-Alone DFIG Applications With Nonlinear Loads”, IEEE Transactions on Power Electronics, vol. 26, no. 9, pp. 2662-2675, 2011.

[49] S.Z. CHEN, N. C. CHEUNG, K. C. WONG, and J. WU “Integral Sliding-Mode Direct Torque Control of Doubly-Fed Induction Generators Under Unbalanced Grid Voltage”, IEEE Transactions on Energy Conversion, vol. 25, no. 2, pp.356-368, 2010.

[50] Y.-K. WU and W.-H. YANG, “Different control strategies on the rotor side converter in DFIG-based wind turbines”, Energy Procedia, vol. 100, pp. 551-555, 2016.

[51] A.WIAM*, H. ALI, “Direct torque control-based power factor control of a DFIG”, Energy Procedia, vol. 162, pp. 296–305, 2019.

[52] P. XIONG and D. SUN, “Backstepping-based DPC Strategy of Wind Turbine Driven DFIG under Normal and Harmonic Grid Voltage”, vol. xx, no. xx, pp. xx-xx, 2015, DOI 10.1109/TPEL.2015.2477442.

[53] L. XIONG, J. WANG, X. MI, and M. W. KHAN, “Fractional Order Sliding Mode Based Direct Power Control of Grid-Connected DFIG”, vol. xx, no. xx, pp. xx-xx, 2017, DOI 10.1109/TPWRS.2017.2761815.

[54] M. BENBOUZID, B. BELTRAN, H. MANGEL and A. MAMOUNE, “A High-Order Sliding Mode Observer for Sensorless Control of DFIG-Based Wind Turbines”, 2012, DOI 978-1-4673-2421-2/12.

[55] A. TOHIDI, H. HAJIEGHRARY and M. A. HSIEH, “Adaptive Disturbance Rejection Control Scheme for DFIG-Based Wind Turbine: Theory and Experiments”, IEEE Transactions on Industry Applications, vol. xx, no. xx, pp. xx-xx, 2015.

[56] A. MERABET , H. ESHAFT, A. A. TANVIR, “Power-current controller based sliding mode control for DFIG-wind energy conversion system”, IET Renewable Power Generation, vol. 12, no. 10, pp. 1155-1163, 2018.

[57] A. ABDELBASET, A.-H. M. El-SAYED, and A. E. H. ABOZEID, “Grid synchronization enhancement of a wind driven DFIG using adaptive sliding mode control”, IET Renewable Power Generation, vol. 11, no. 5, pp. 688-695, 2017.

[58] H. MORADI, Y. A-BEROMI, H. Y. and D. BUSTAN, “Sliding mode type-2 neuro-fuzzy power control of grid-connected DFIG for wind energy conversion system”, IET Renewable Power Generation, vol. 13, no. 13, pp. 2435-2442, 2019.

[59] L. GUO, D. WANG, Z. PENG and L. DIAO, “Improved super-twisting sliding mode control of a stand-alone DFIG-DC system with harmonic current suppression”, IET Power Electronics, vol. 13, no. 7, pp. 1311-1320, 2020.

[60] M. BOUTOUBAT, L. MOKRANI and M. MACHMOUM, “Control of a wind energy conversion system equipped by a DFIG for active power generation and power quality improvement”, Renewable Energy, vol. 50, pp. 378-386, 2013.

[61] M. E. ZAREI, C. V. NICOLÁS and J. R. ARRIBAS, “Improved Predictive Direct Power Control of Doubly Fed Induction Generator during Unbalanced Grid Voltage Based on Four Vectors”, IEEE Journal of Emerging and Selected Topics in Power Electronics, vol. xx, no. xx, pp. xxx-xxx, 2016.

[62] A. JAIN, V. RANGANATHAN, “Wound rotor induction generator with sensorless control and integrated active filter for feeding nonlinear loads in a stand-alone grid”, IEEE Trans. Ind. Electron., 2008, 55, (1), pp. 218–228.

[63] F. AMRANE, B. FRANCOIS and A. CHAIBA, ”Hardware Implementation study of Variable Speed Wind-Turbine-DFIG in Stand-alone Mode”, 22nd European Conference on Power Electronics and Applications (EPE'20 ECCE Europe), Lyon-FRANCE, 7-11 Sept. 2020

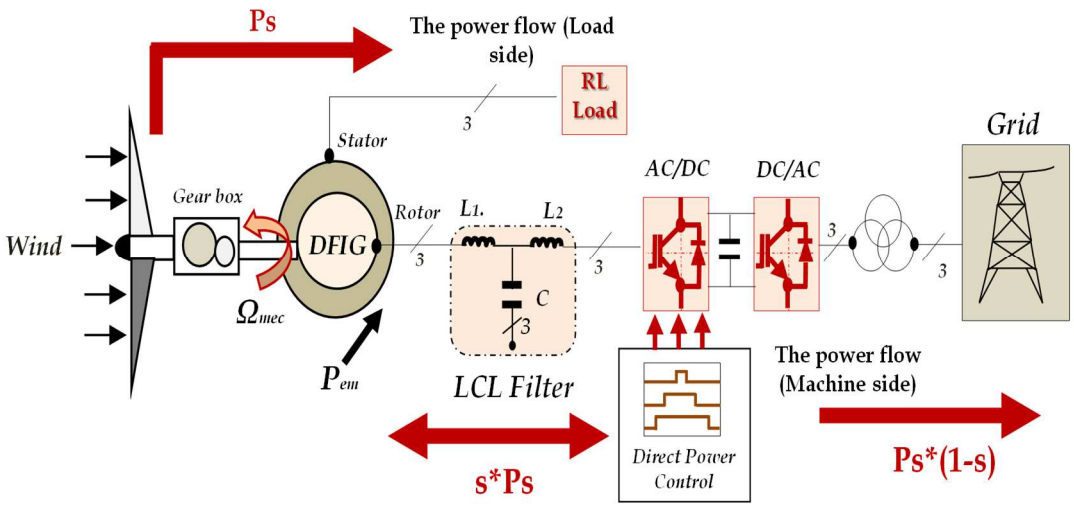

Fig.1-Schematic diagram of DFIG using direct power control in stand-alone mode.

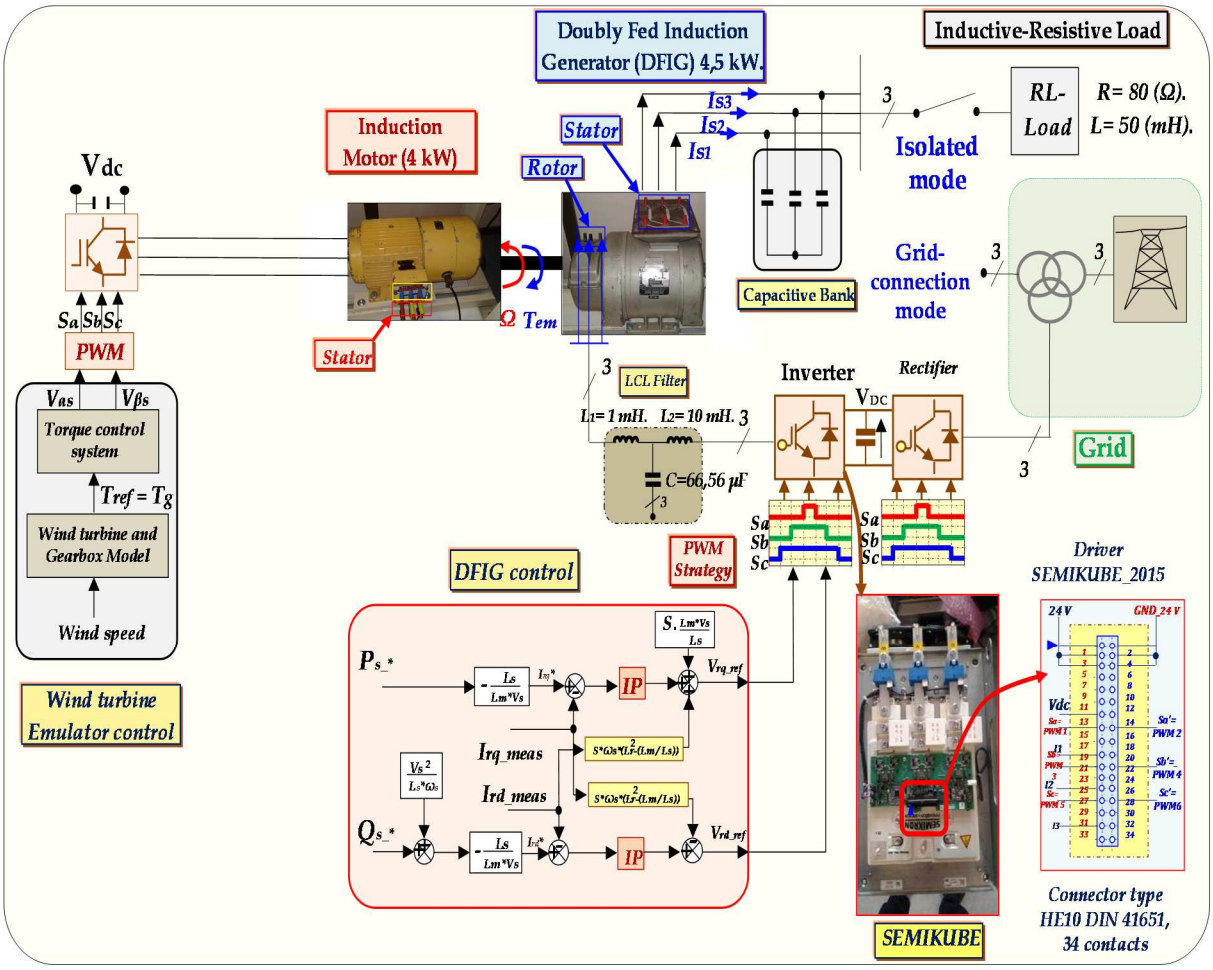

Fig.2-Proposed control scheme based on DFIG power control in stand-alone mode.

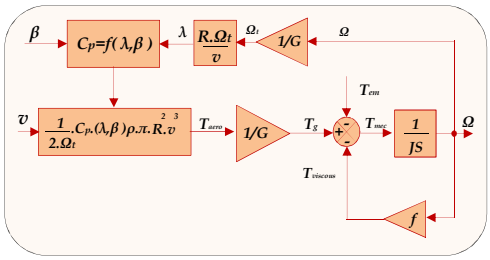

Fig.3-Schematic block of wind turbine.

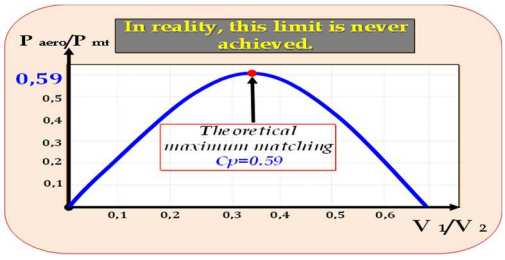

Fig.4-Theorical maximum power coefficient (Cp= (16/27) ≈ 0.59).

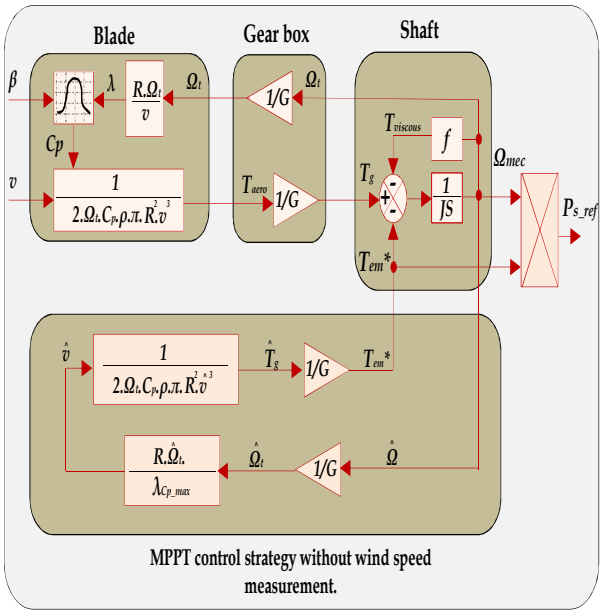

Fig.5-MPPT control strategy without wind speed measurement.

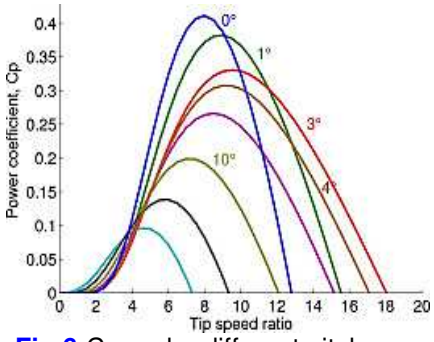

Fig.6-Cp under different pitch angles (B°).

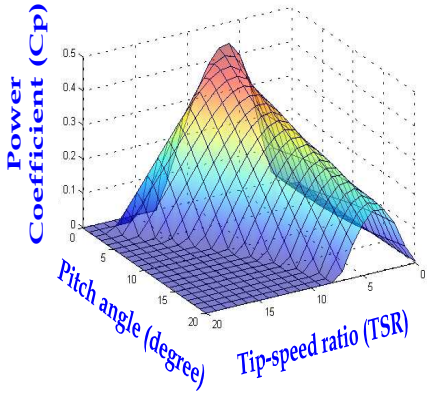

Fig.7-3D Power coefficient versus Tip speed ratio (TSR) and Pitch angle degree (B°).

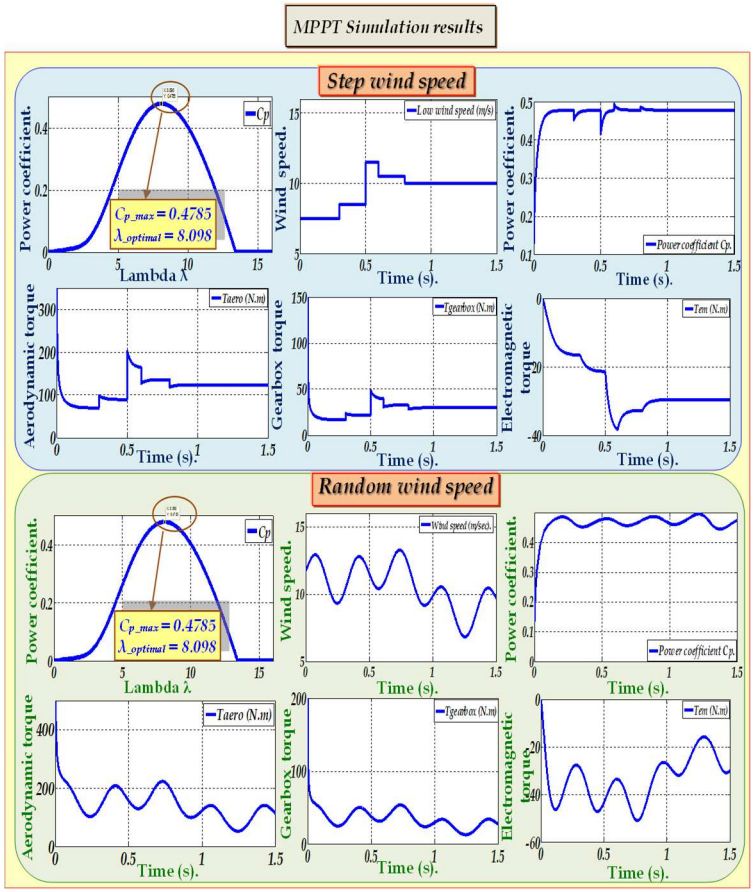

Fig.8-Simulation results of MPPT strategy: (C_p versus λ "or TSR", Wind speed versus time, C_p versus time) T_{aero}, $T_{gearbox}$ & T_{em} using two wind speed profiles.

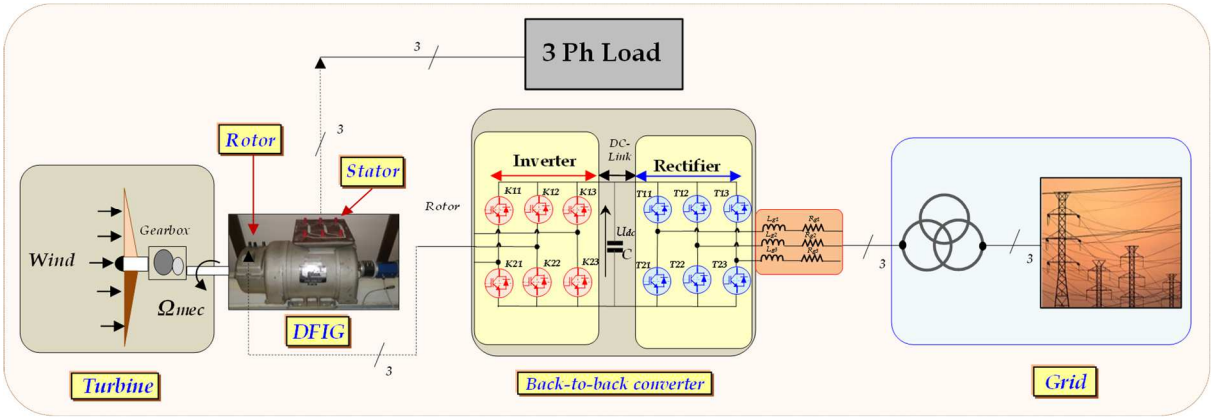

Fig.9-Main circuit topology of a back-to-back PWM converter fed DFIG (stand-alone mode).

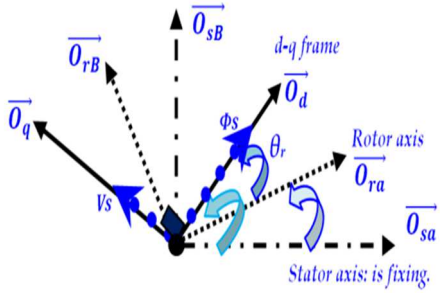

Fig.10-Stator and rotor flux vectors in the synchronous d-q frame.

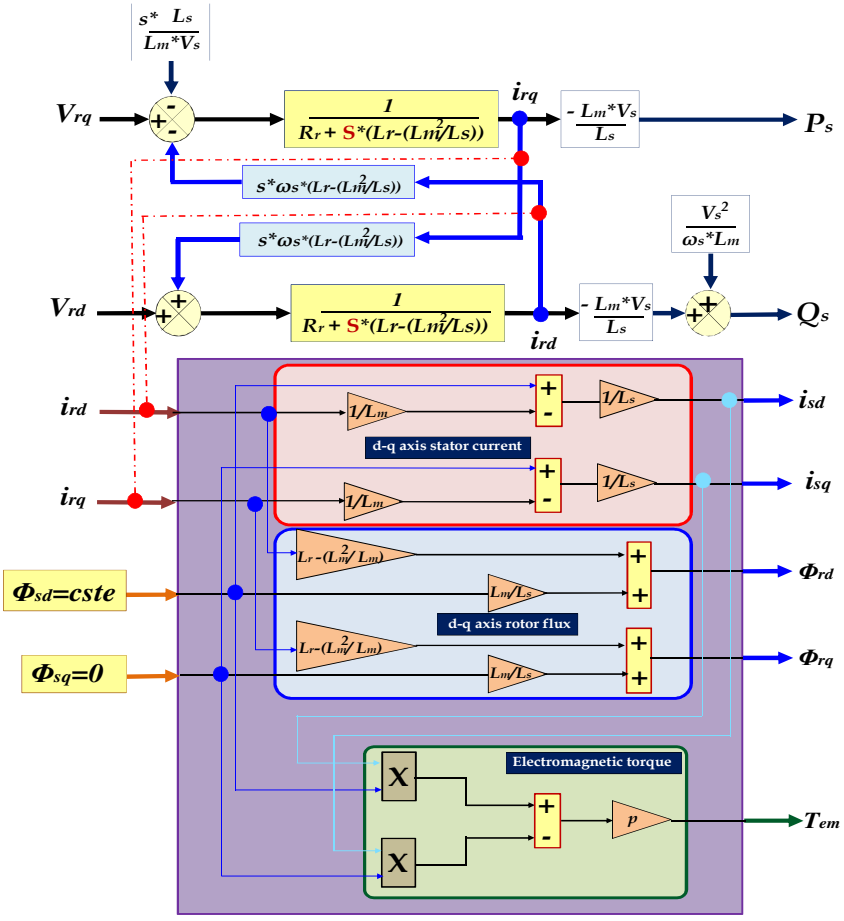

Fig.11-The doubly fed induction generator simplified model.

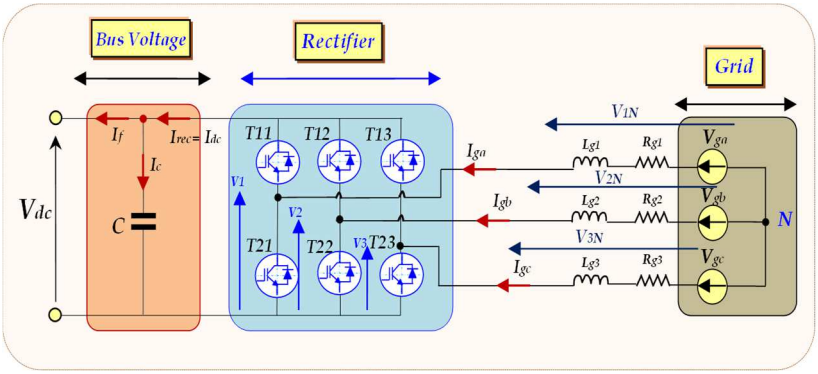

Fig.12-GSC configuration.

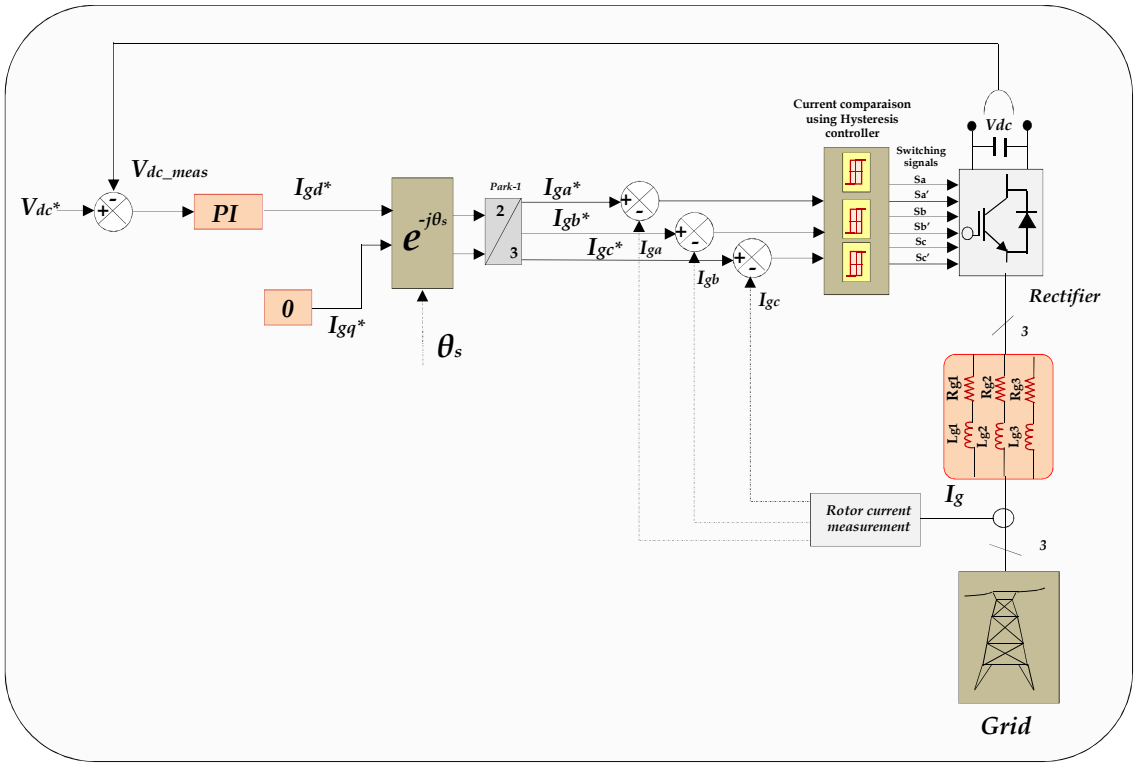

Fig.13-Grid side converter topology (DC-link voltage control).

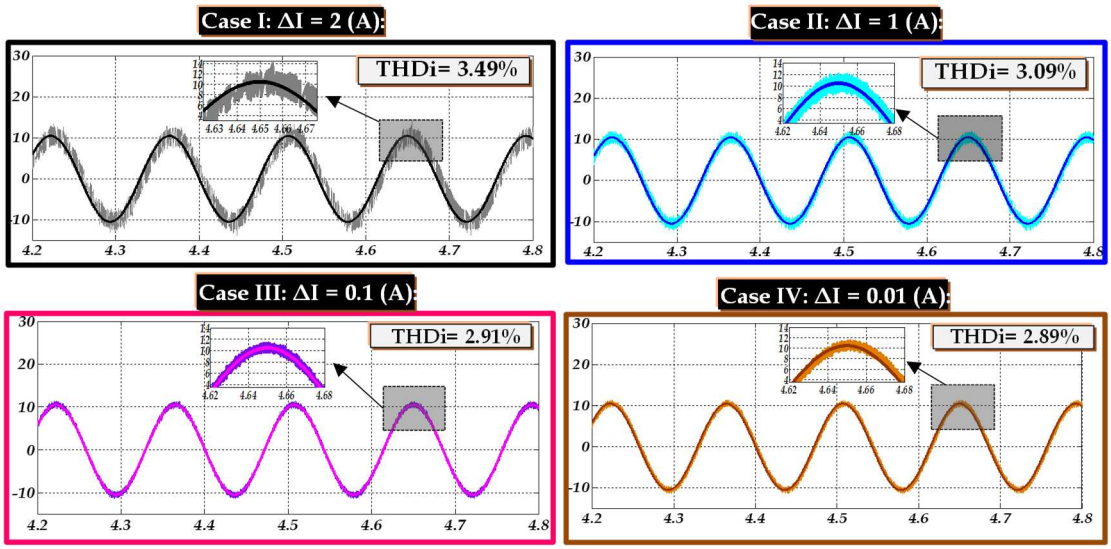

Fig.14-Impact of the hysteresis band in grid current control (Grid side converter).

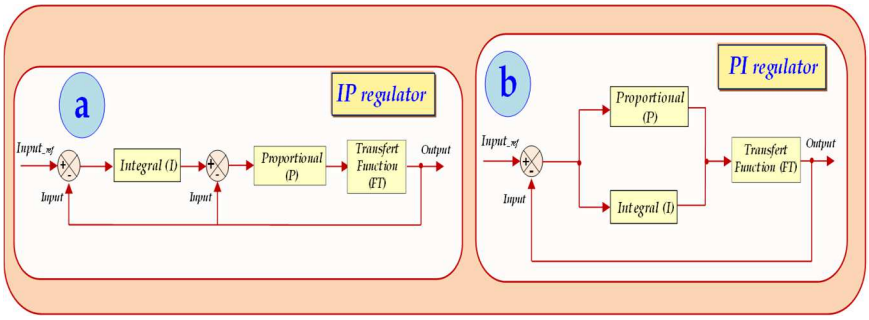

Fig.15-Schematic diagram of IP and PI regulators.

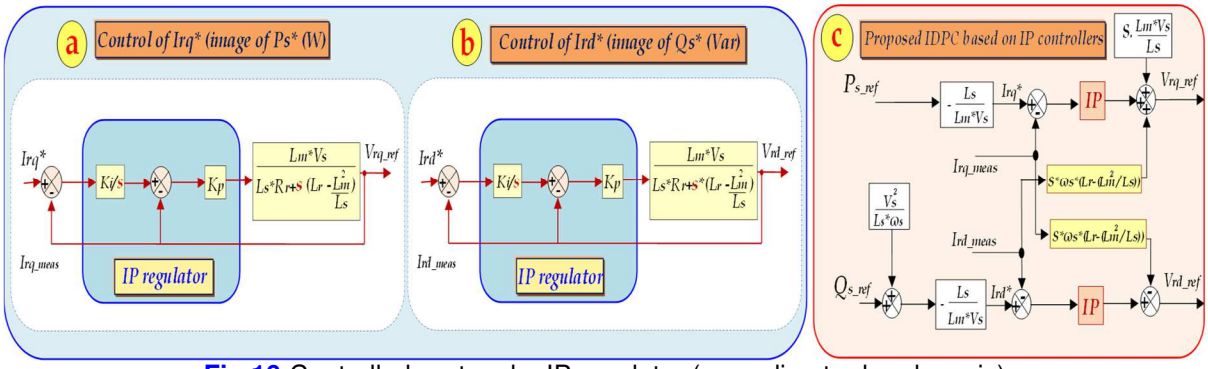

Fig.16-Controlled system by IP regulator (according to d and q axis).

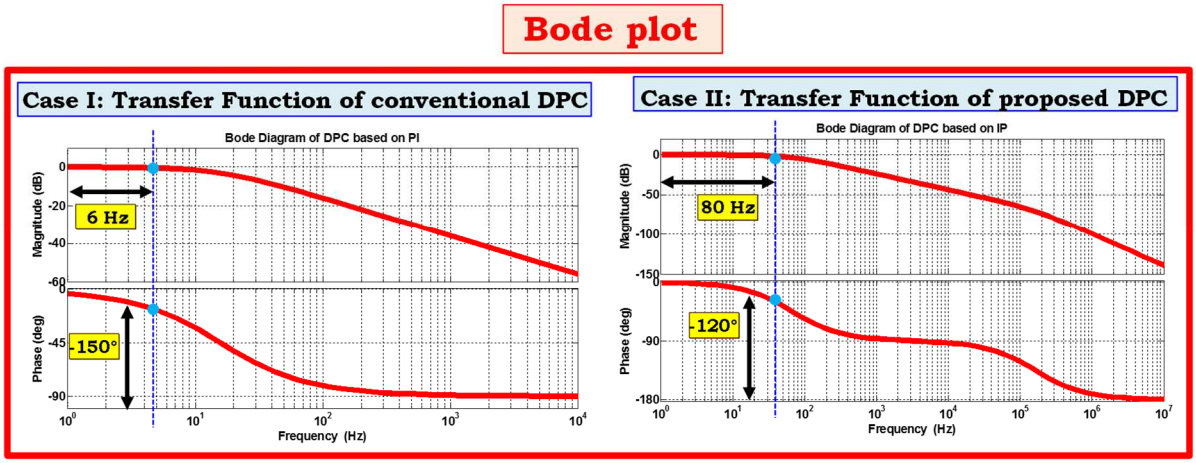

Fig.17- Frequency responses based on Transfer function plot for conventional and proposed control using Bode plot.

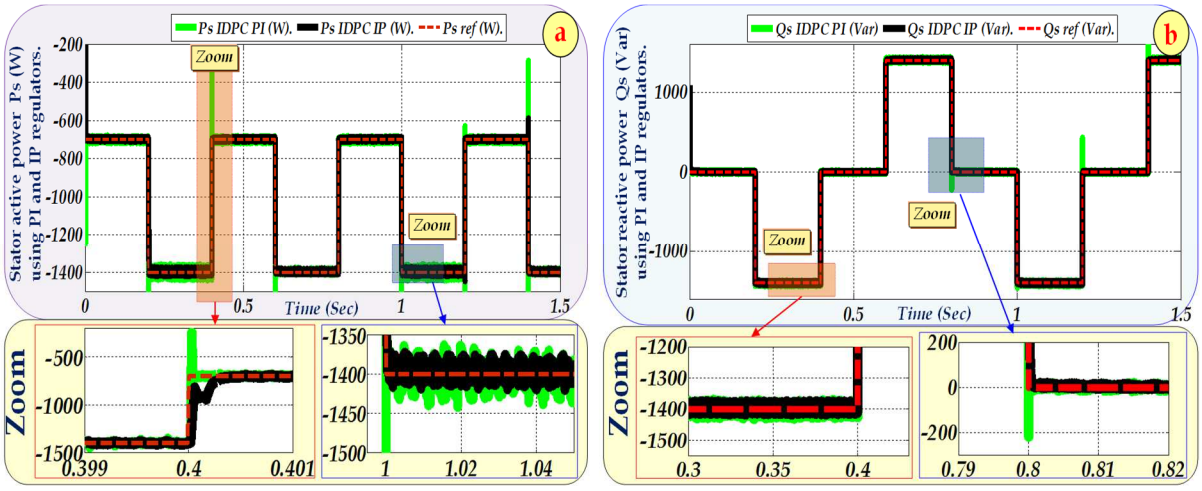

Fig.18-(a and b): The stator active and reactive power controlled by 'PI and IP' controllers respectively.

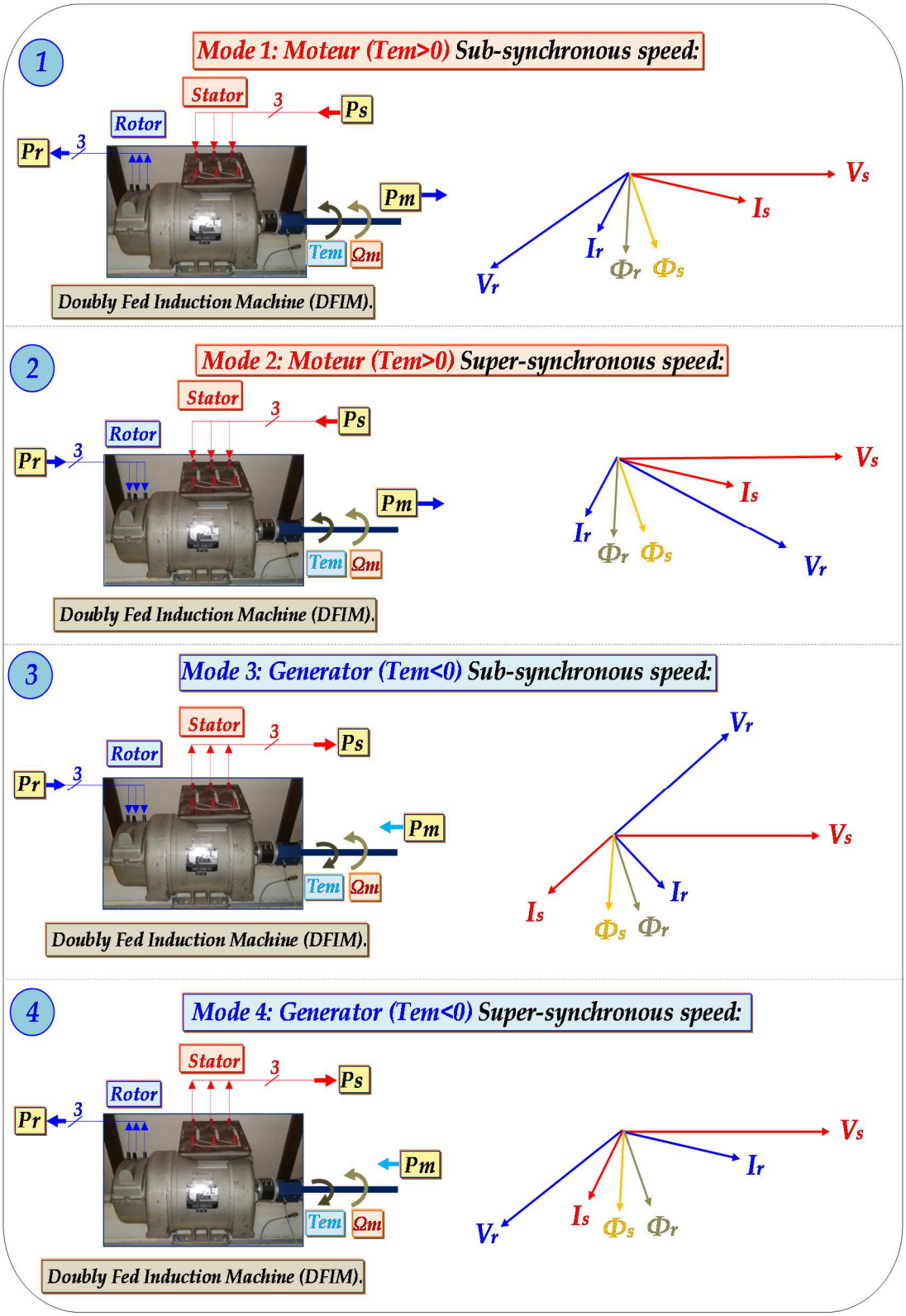

Fig.19-Power-flow diagram of a DFIM for (1): Sub-synchronous motoring mode, (2): Super-synchronous motoring mode, (3): Sub-synchronous generating mode, and (4): Super-synchronous generating mode.

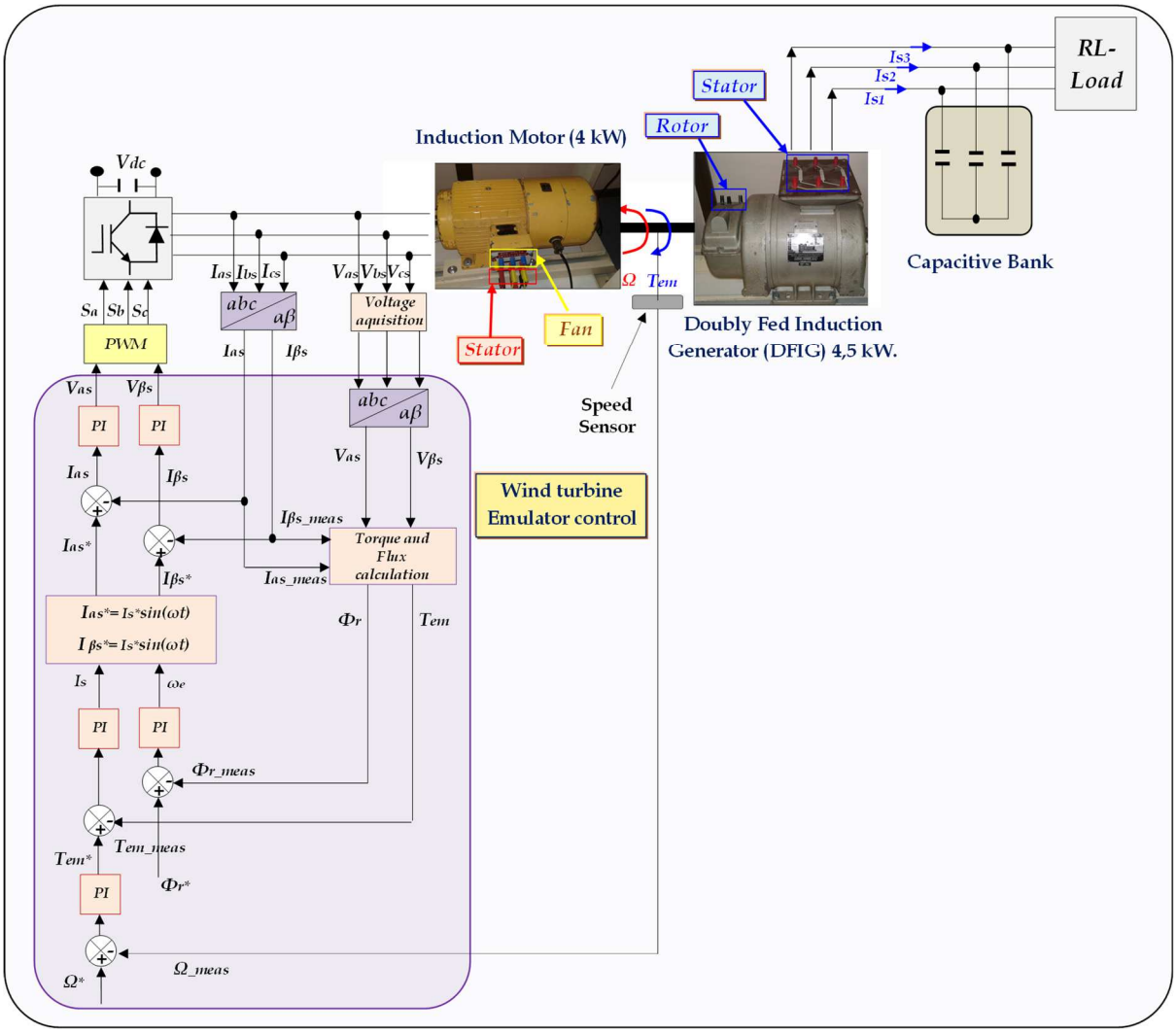

Fig.20-Induction motor torque and rotor flux control system.

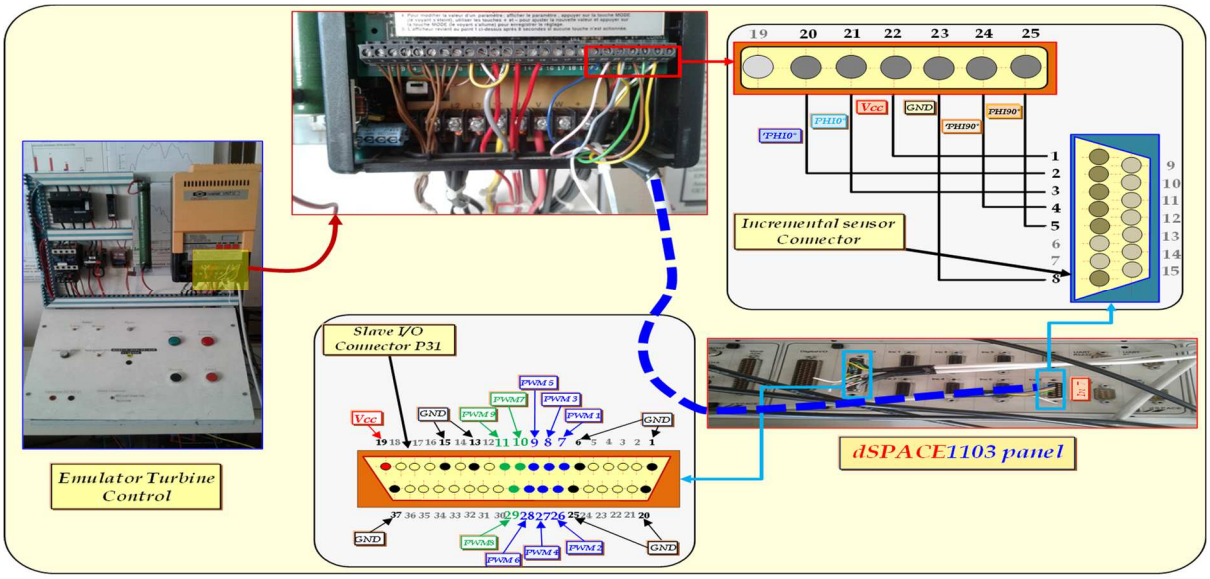

Fig.21-Hardware connexion of emulator wind turbine and dSPACE1103 panel via incremental sensor connector.

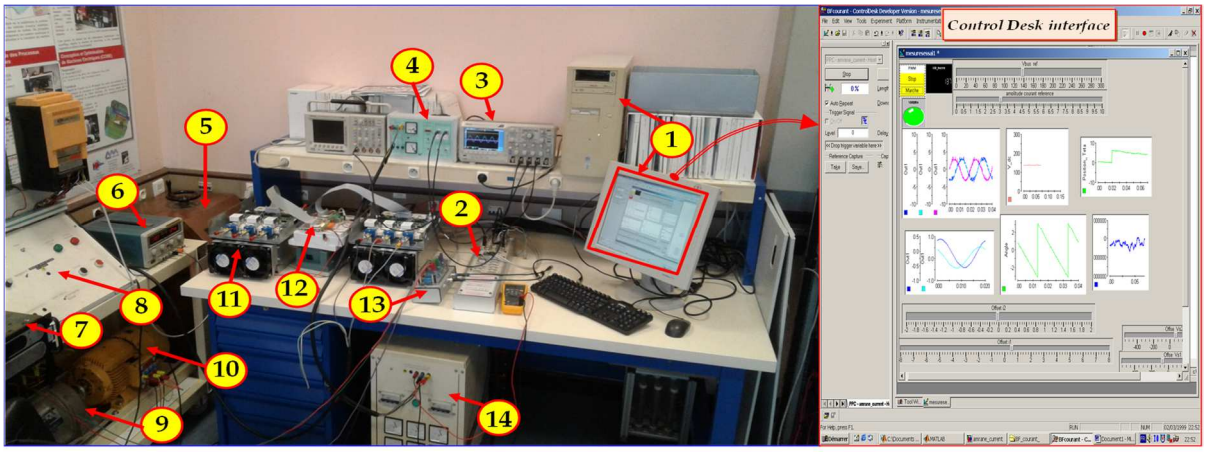

Fig.22-Experimental test bench developed in L2EP Laboratory.

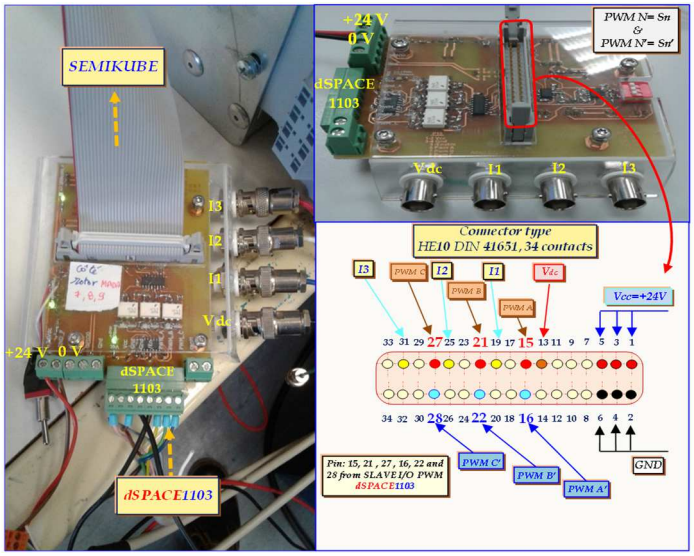

Fig.23-The isolation card used between the SEMIKUBE and the panel dSPACE-1103.

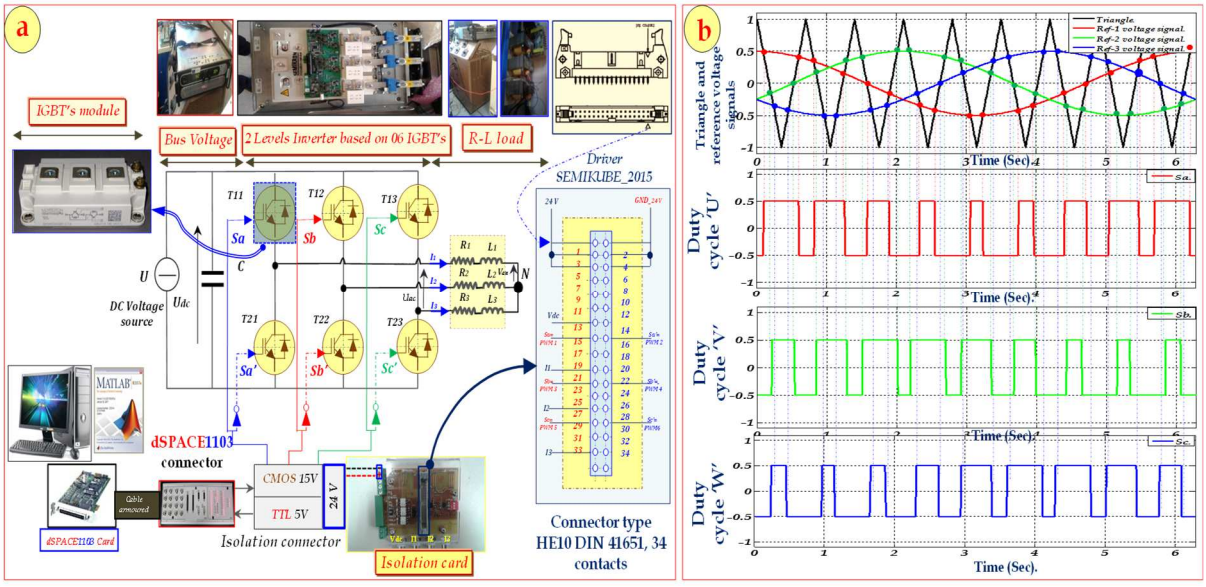

Fig.24-a: Open loop hardware scheme using SEMIKUBE with R-L Load (Stand-alone) and b: PWM signals for three SEMIKUBE Legs.

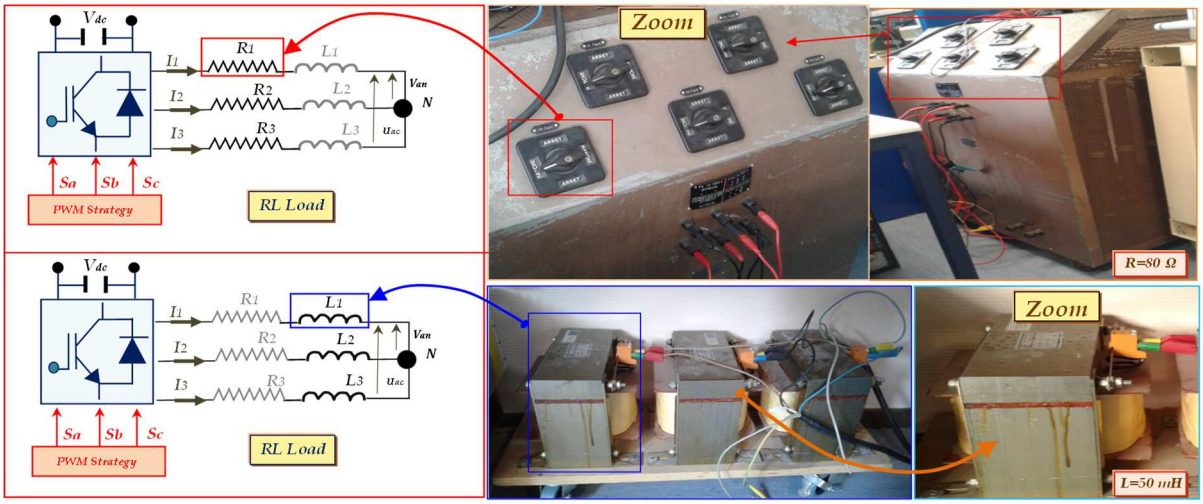

Fig.25-The R-L load used in SEMIKUBE' performance tests.

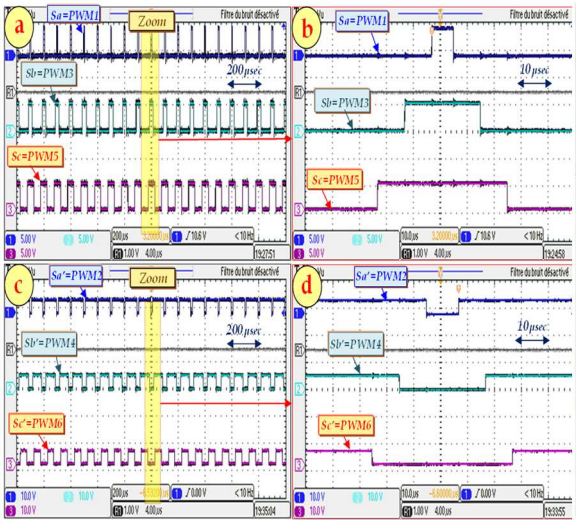

Fig.26-Switching signals: high (Sa, Sb and Sc) and low (Sa', Sb' and Sc').

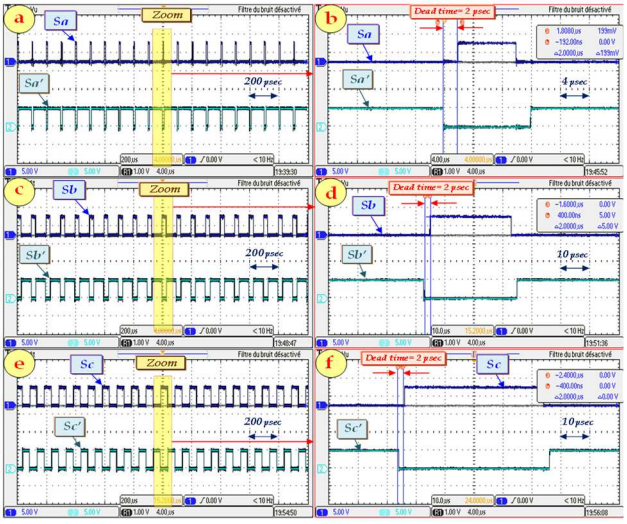

Fig.27-Dead time between the switching signals for each leg.

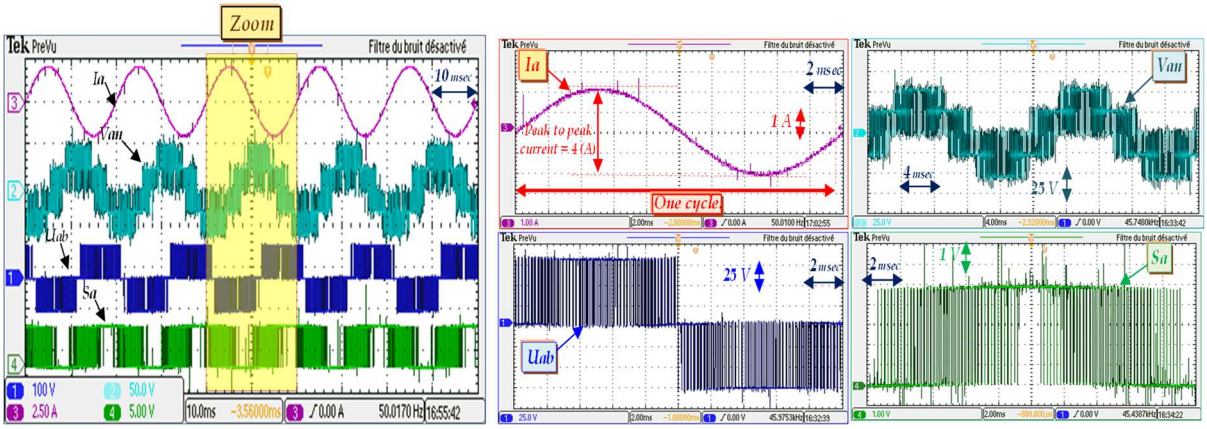

Fig.28-Current and voltage waveforms of RL-load under V_{dc}= 80 (V).

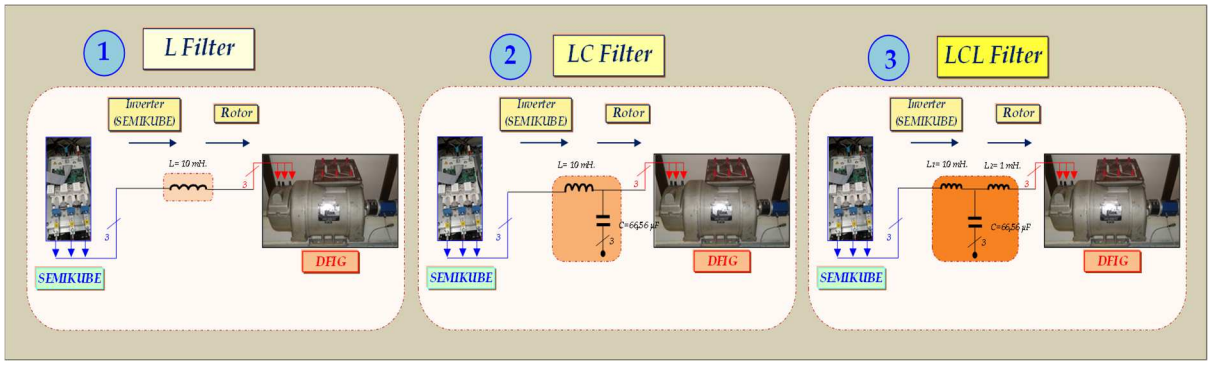

Fig.29-Proposed filters (L, LC and LCL) topologies.

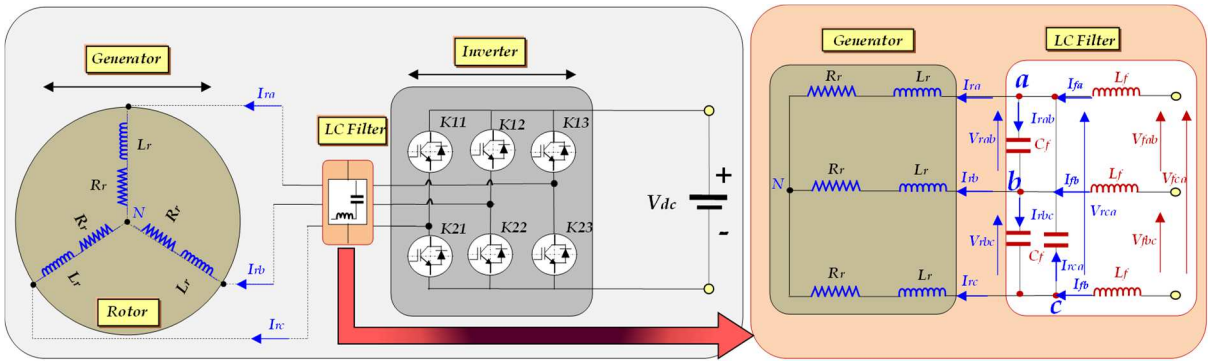

Fig.30-Rotor side converter topology with LC-Filter.

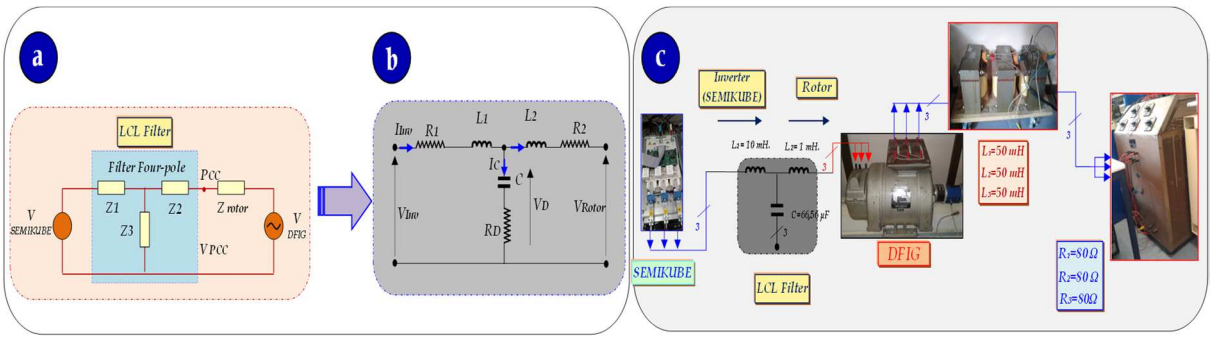

Fig.31-Single phase LCL-Filter schematic.

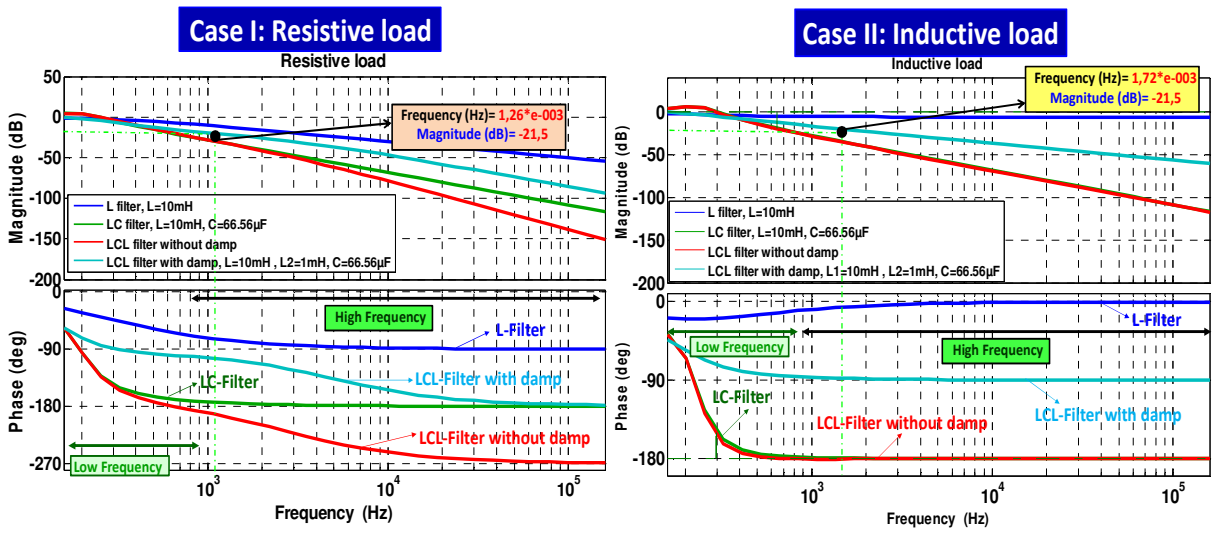

Fig.32-Bode plot of three transfer function filters “L, LC and LCL” for resistive and inductive load.

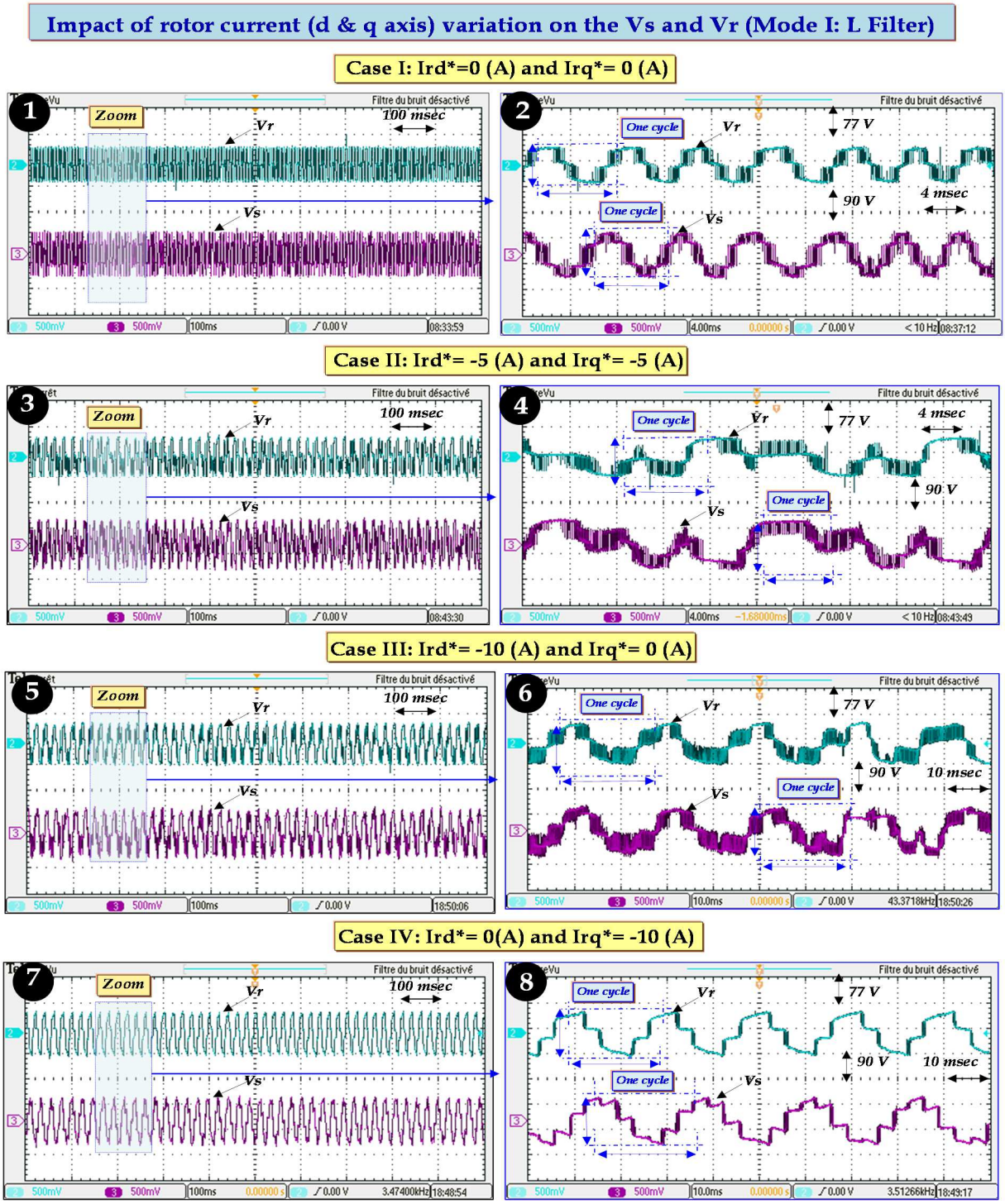

Fig.33-Experimental results of the rotor' and stator voltages waveforms (under d-q axes rotor currents variation using L-type Filter).

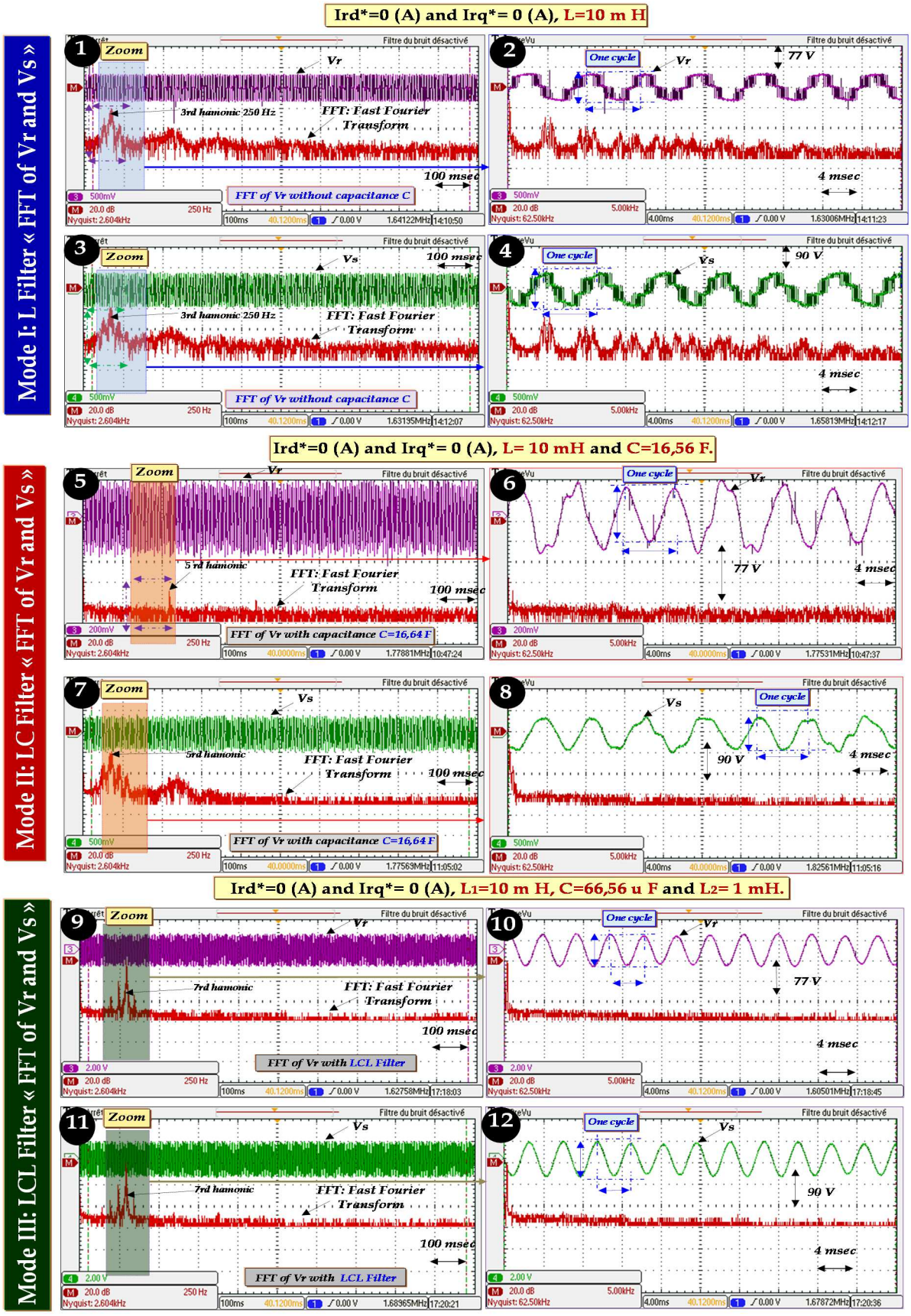

Fig.34-Experimental results of the rotor' and stator voltages using FFT (without rotor currents variation using L, LC and LCL-type Filters respectively).

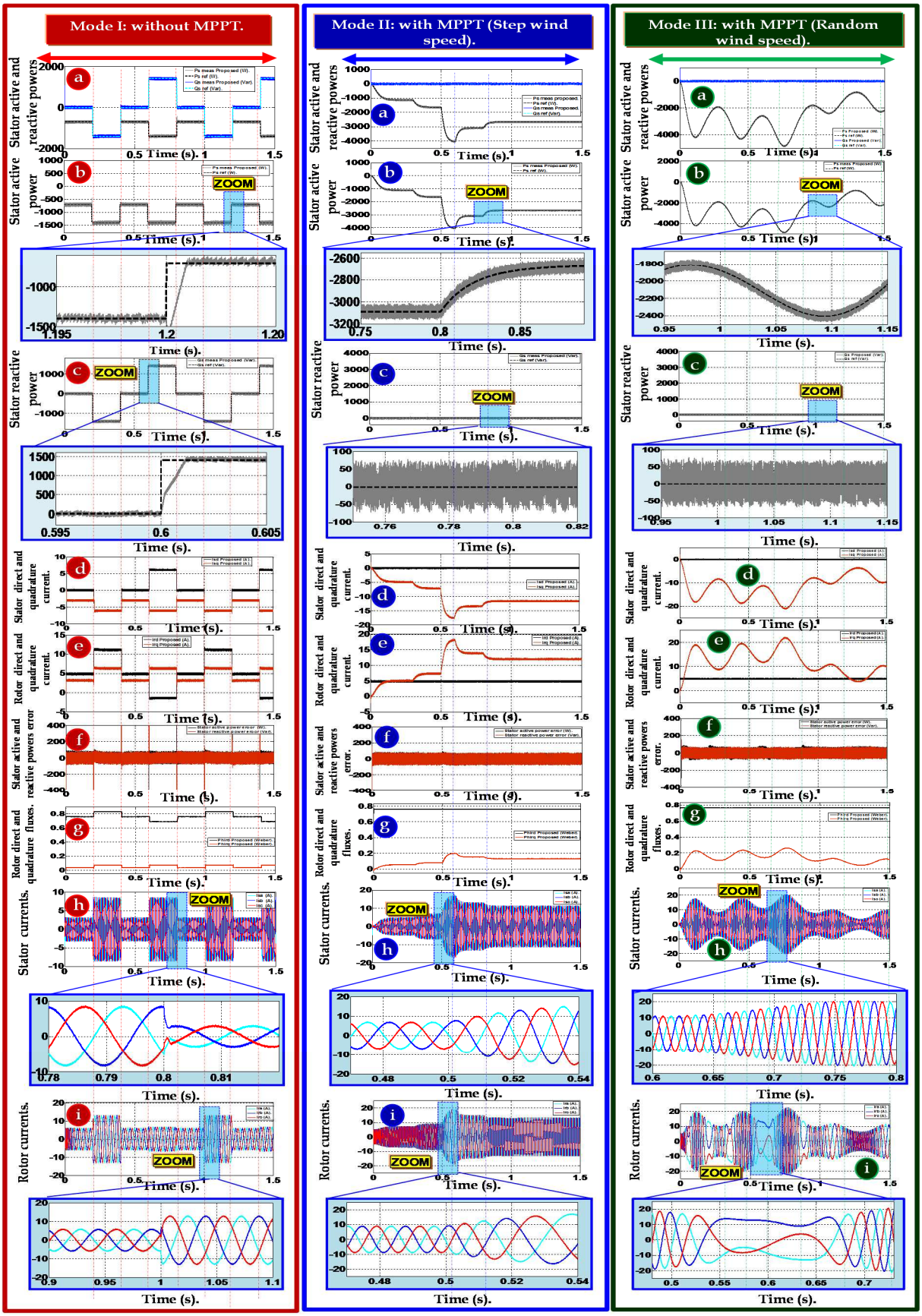

Fig.35-Simulation results of proposed control under Modes:1, 2 & 3 (a): stator active and reactive powers, (b): stator active power, (c): stator reactive power, (d): stator direct and quadrature currents, (e): rotor direct and quadrature currents, (f): stator active and reactive power error, (g): rotor direct and quadrature fluxes, (h): stator currents, (i): rotor currents.

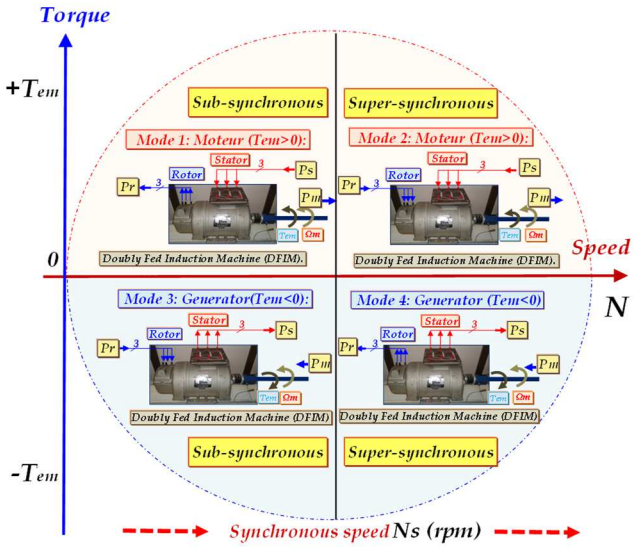

Fig.36-The power-flow of the DFIG under four (04) quadrants.

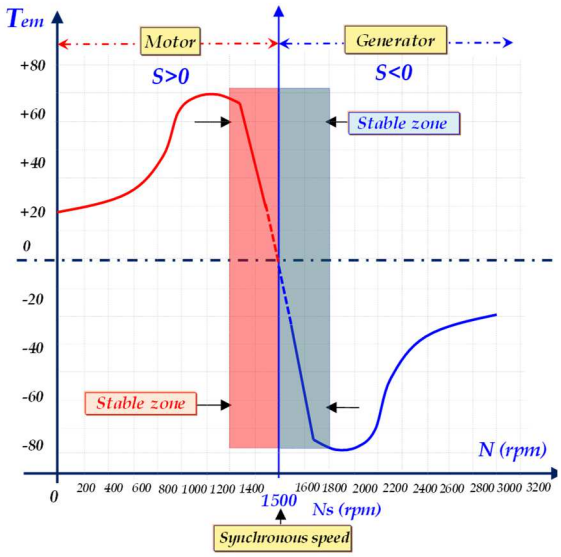

Fig.37- The Torque/speed characteristic of the DFIG.

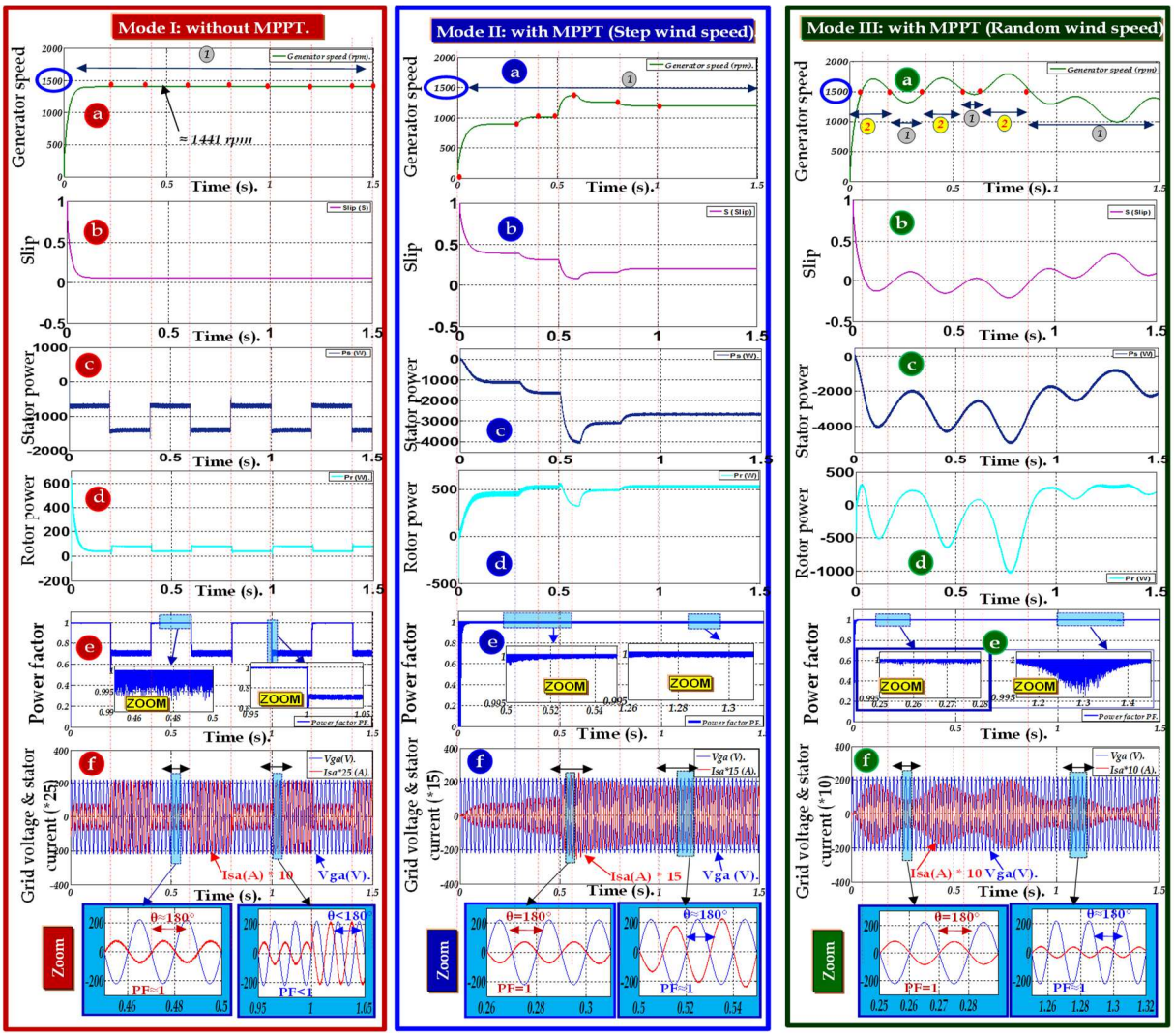

Fig.38-Simulations results of proposed control: Power factor study (a: generator speed, b: slip, c: stator power, d: rotor power, e: power factor and f: grid voltage and stator current).

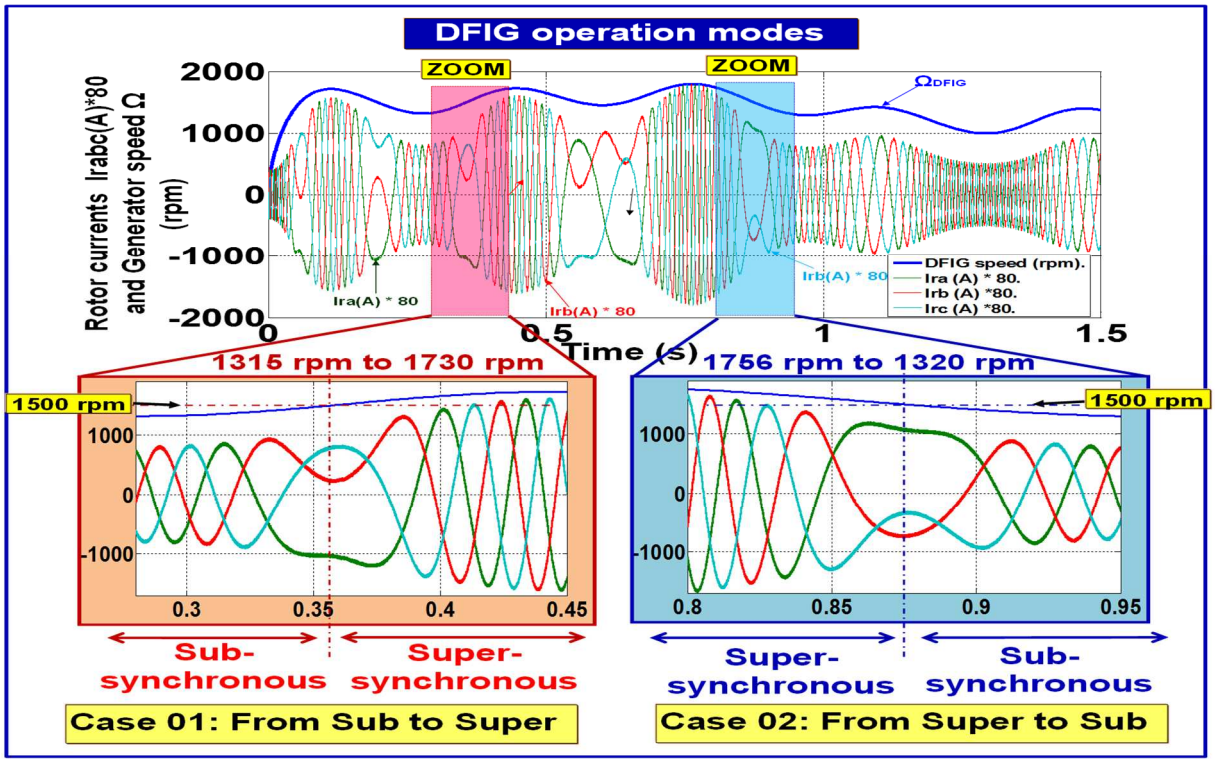

Fig.39-Simulations results of DFIG operation modes (a: Sub-synchronous operation, b: Super-synchronous)

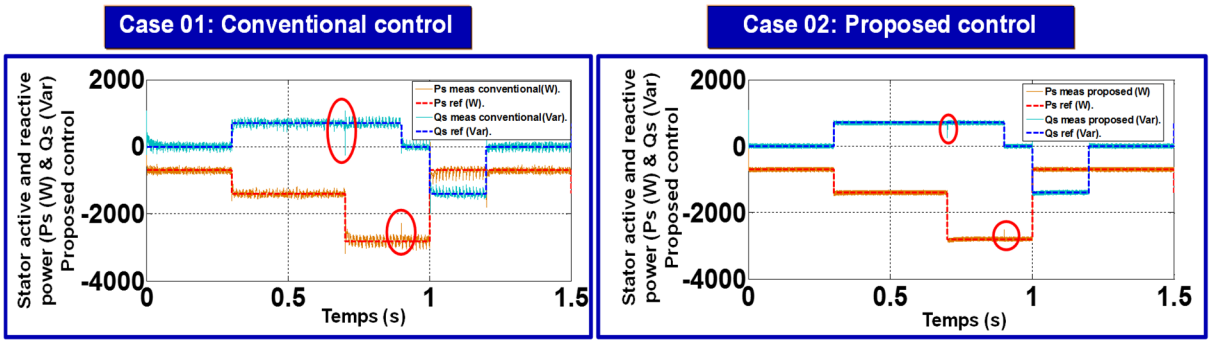

Fig.40-Simulations results of decoupled terms performance (The stator active and reactive power for conventional and proposed control respectively).

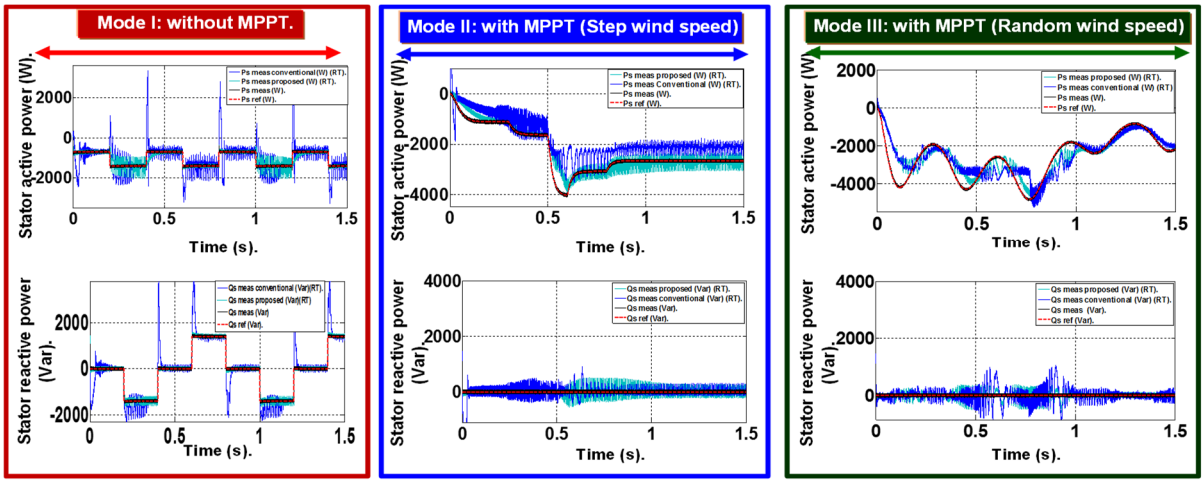

Fig.41- Robustness tests of proposed control of P_s and Q_s for three modes.

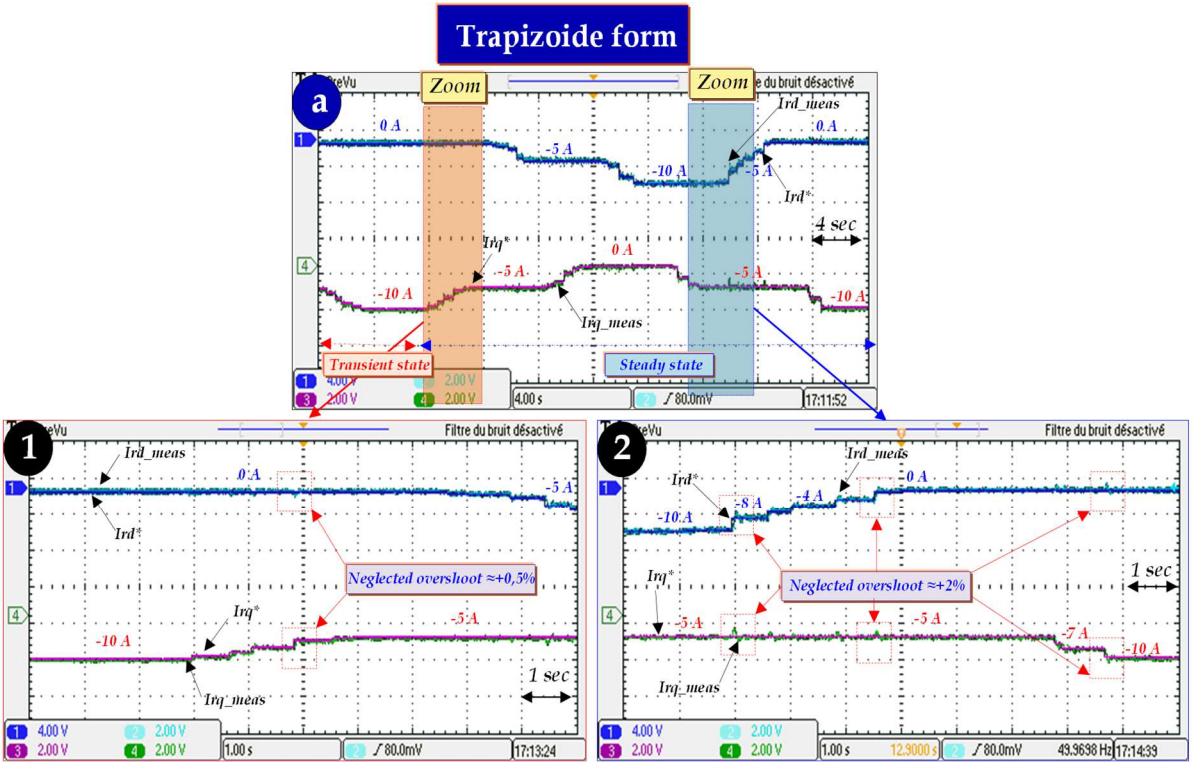

Fig.42-(a, 2 and 3) Robustness tests under trapezoid forms (rotor currents variation with RL-load).

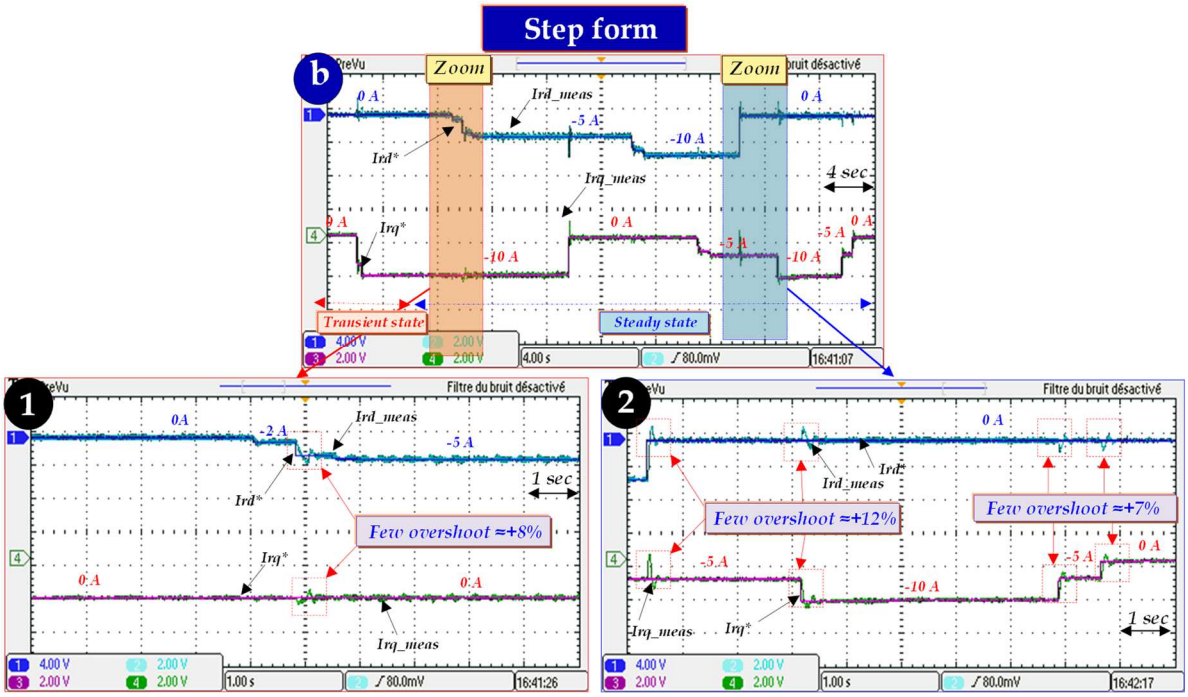

Fig.43-(b, 2 and 3) Robustness tests under trapezoid forms (rotor currents variation with RL-load).

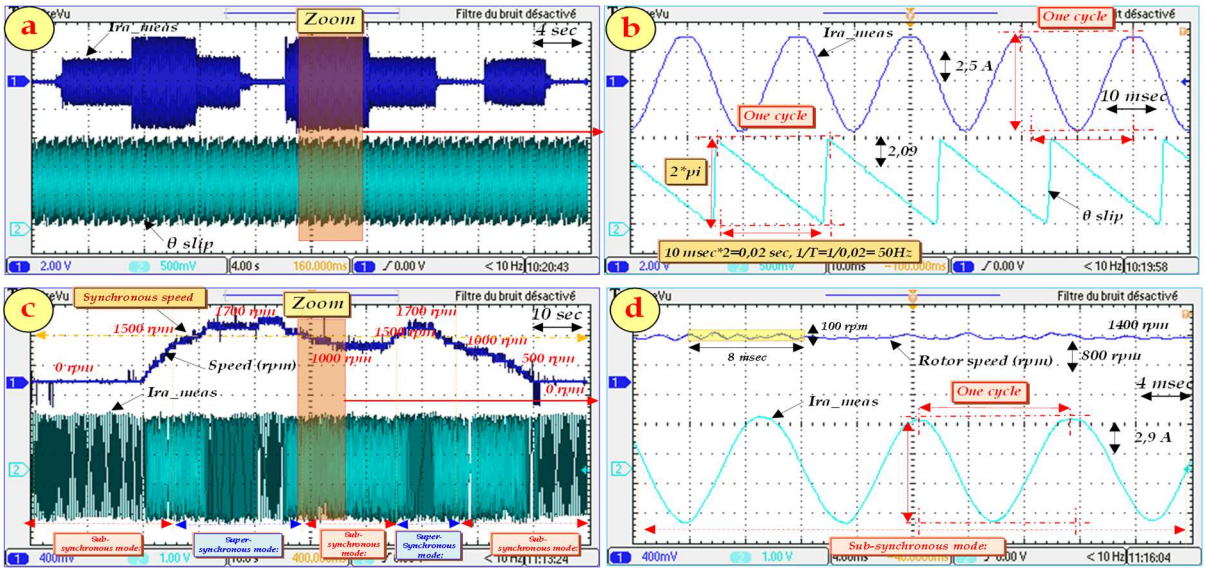

Fig.44-(a and b): Measured rotor current variation and slip angle, (c and d): Rotor speed variation and measured rotor.

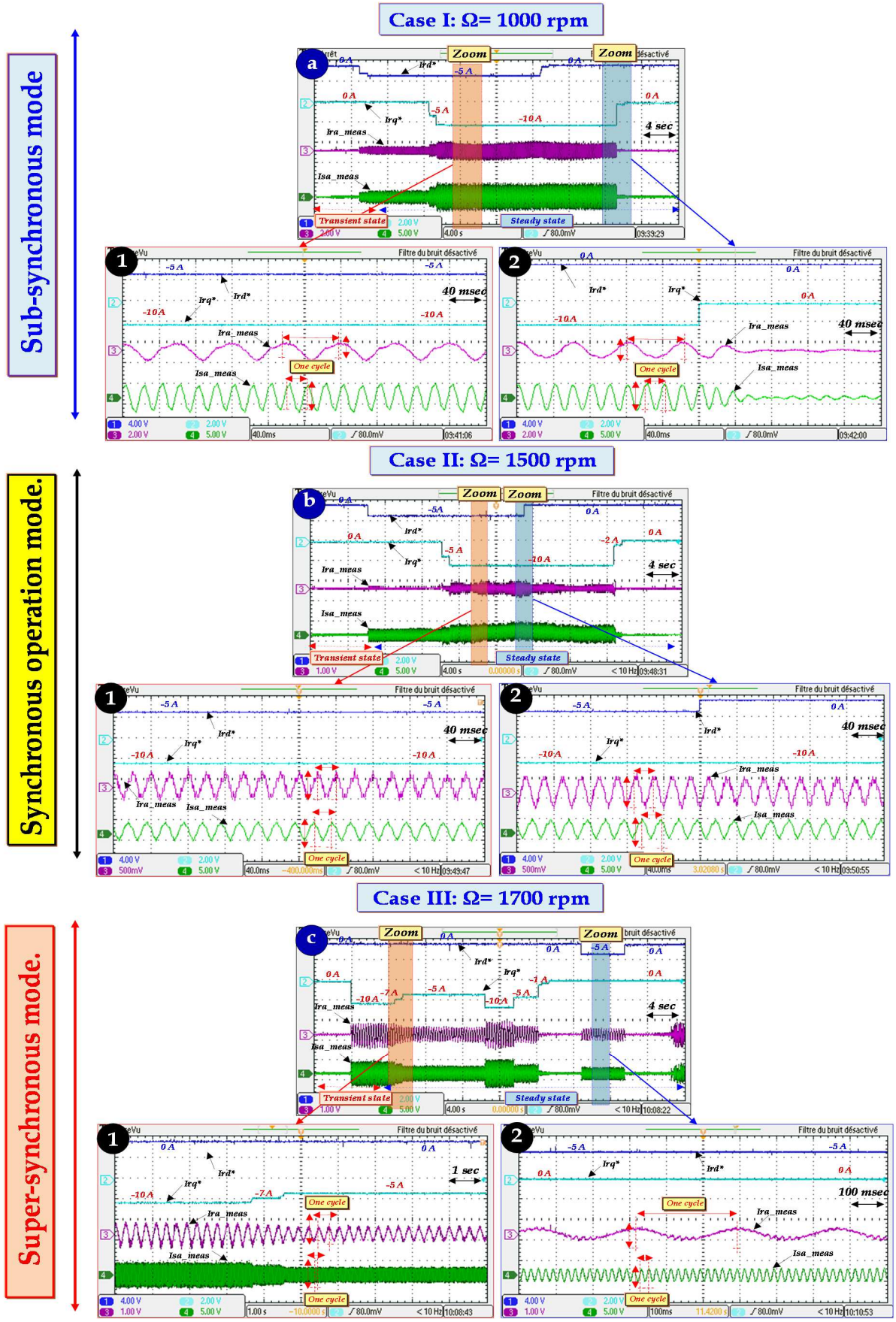

Fig.45-Rotor speed variation and measured rotor current under three operation mode (Case 01 N = 1000 rpm, Case 02: N=Ns=1500 rpm and Case 03: N=1700rpm).

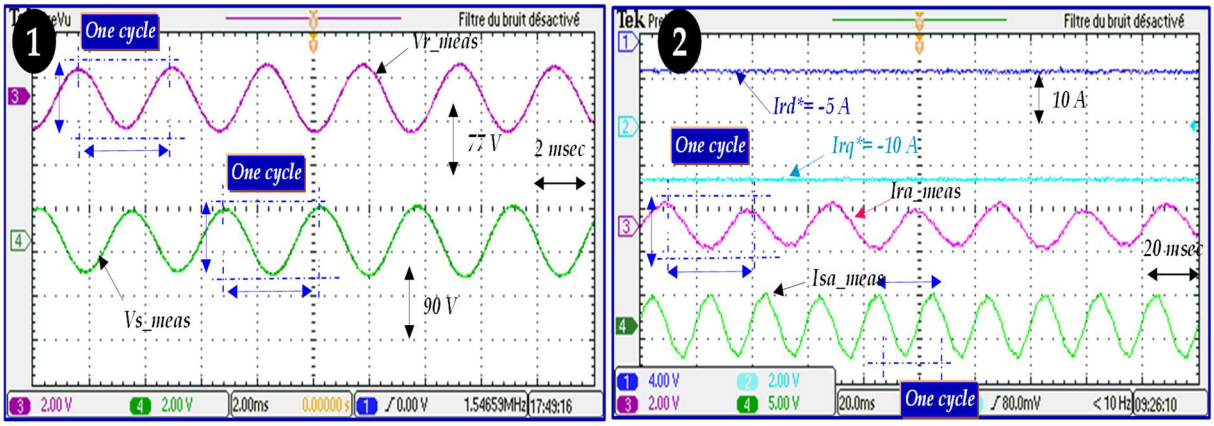

Fig.46-(1 and 2): The stator and rotor voltages waveforms.

Table.1-Comparative study of power control performances using PI & IP respectively.

Criteria: / Controller:	Power tracking:	Power Error (W_Var):	Overshoot (%):	Dynamic response (s)	Sensevity to parameter changement:
DPC based on PI controller:	Good	60 W_Var	Remarkable ≈20%	Fast $T_{r\_PI}=4.5*10^{-5}$	High
DPC based on IP controller:	Excellent	45 W_Var	Neglected near ≈1%	Medium $T_{r\_IP}=50*10^{-5}$	Medium

Table.2 Parameters of R-L load under open loop tests:

Parameter:	Value:
DC voltage (V_{DC})	**80 (V).**
Switching frequency	**f_{s_Test}= 5 K (Hz).**
Load current :	**I_{0_Test}= 4 (A)**
Rated load power	**P = 1,28 K (W).**
Load resistance:	**R_{0_Test}= 80 (Ω)**
Load inductance:	**L_{0_Test} = 50 m (H)**

Table.3 LCL filters' element with their values.

LCL components:	Parameter Description
V_{Inv}	Voltage inverter (SEMIKUBE).
V_{Rotor}	Rotor voltage (80 (V))
I_{Inv}	Inverter current (A).
Ic	Capacitance current (A).
I_{Rotor}	Rotor current (10 (A)).
L_1	Inverter side inductor (10 (mH)).
L_2	Rotor side inductance (1 (mH)).
R_1	Inverter side resistance (0.5 (Ω)).
R_2	Rotor side resistance (0.2 (Ω)).
R_D	Damping resistance (0.3 (Ω)).
C	Capacitance (66.56 (µF)).

Table.4 Bode plot application for four (04) transfer function filters

Cases:	Transfer function order:	Type-Filter studied in the case of the resistive and inductive load:
Case 1:	1st order	L-type Filter ⇒ Dark blue
Case 2:	2nd order	LC-Type Filter ⇒ Green
Case 3:	3rd order	LCL-Type Filter without damp ⇒ Red
Case 4:	3rd order	LCL-Type Filter with damp ⇒ Sky blue

Table.5 References rotor current variation using L-filter.

Cases:	Reference rotor current variation (I_{rd}* and I_{rq}*):	Voltages:
Case 1:	I_{rd}*= 0(A) and I_{rq}*= 0(A).	For all cases⇒ Vr= 77 (V) Vs= 90 (V)
Case 2:	I_{rd}*= -5 (A) and I_{rq}*= -5 (A).	
Case 3:	I_{rd}*= -10 (A) and I_{rq}*= 0 (A).	
Case 4:	I_{rd}*= 0 (A) and I_{rq}*= -10 (A).	

Table.6 Impact of passive filter in Wind-turbine DFIG system (simulation and experimental studies).

Performance / Filter types	Reference	Parameter values:	Location filter:	Study nature:	Equation model:	THDi% / THDv%	Power rated
L-filter	[4]	L=500 µH	GSC	Experimental	1st order	-	7.5 KW
	[37]	L=3.8 mH	GSC	Experimental	1st order	THD_i =1.34%	3.7 KW
	[38]	L=3.8 mH	GSC	Experimental	1st order	-	S=185 VA
	Proposed	L= 10 mH.	RSC	Experimental	1st order	THD_i =5.5%	4 KW
LC-filter	[39]	L=24 mH, C=40 µf (based on SEGI)	GSC	Experimental	2nd order	THD_i =2.67%	250 W
	[40]	L=20 mH, C=69 uF	GSC	Experimental	2nd order	THD_i =9.0 %	7.5 KW
	Proposed	L=10 mH, C=66.56 uF	RSC	Experimental	2nd order	THD_i=3.5%	4 KW
LCL-filter	[4]	L_C=125 µH, C_F= 220 µF, L_F=125 µH & Rd=0.5 mΩ	GSC	Experimental	3rd order	-	7.5 KW
	[36]	L_1=125 µH, C= 300 uF, L_2=125 µH	GSC	Simulation	3rd order	THDv=10.09%	2 MW
	Proposed	L_1=10 mH, C= 66.56 uF, L_2=1 mH & Rd=0.3 Ω	RSC	Experimental	3rd order	THD_i=1.5%	4 KW

Table.7-The proposed profiles of the active and reactive power references.

Time (sec):	Stator active power (W):	Stator reactive power (Var):
[0 - 0.2]	-700.	0.
[0.2–0.4]	-1400.	-1400.
[0.4–0.6]	-700.	0.
[0.6–0.8]	-1400.	+1400.
[0.8–1.0]	-700.	0.
[1.0–1.2]	-1400.	-1400.
[1.2–1.4]	-700.	0.
[1.4–1.5]	-1400.	+1400.

Table.8-Recapitulation results for the proposed control.

	THD_Is_abc (%):	Overshoot (%):	Respense time (Sec):	Power Error (W_Var) :
Mode 01	01.23 %	Neglected (≈ 2%).	$5* 10^{-4}$.	+/- 45.
Mode 02	0.78 %	Neglected (≈ 1%).	$1,3 * 10^{-3}$.	+/- 65.
Mode 03	0.42 %	Neglected (≈ 1%).	$1,3* 10^{-3}$.	+/- 60.

Table.9-DFIG operation modes parameters

Cases:	DFIG operation mode:
Case 01:	From Sub to Super-synchronous speed: ⇒ 1315 to 1730 rpm
Case 02:	From Super to Sub-synchronous speed: ⇒ 1756 to 1320 rpm

Table.10 The proposed references profiles for decoupled terms performance

Time (sec):	Stator active power (W):	Stator reactive power (Var):
[0 - 0.3]	-700.	0.
[0.3–0.7]	-2000.	+1000.
[0.7–1.0]	-2700.	0.
[1.0–1.2]	-700.	-1400.
[1.2–1.5]	-700.	0

Table.11-The proposed robustness tests.

Control algorithms	Stator active and reactive powers tests:
Proposed control without test:	No parameters changement⇒ Black
Conventional control with test:	+100% of (J and Rr), -25 % of (Lr, Ls and Lm) ⇒ Dark blue.
Proposed control with test:	+100% of (J and Rr), -25 % of (Lr, Ls and Lm) ⇒ Sky blue.

Table.12 A comparative study of different control schemes based on DFIG-Wind Turbine variable speed.

Ref	Control scheme:		Comple-xity	DFIG rated power	Reference tracking:	Overshoot:	Dynamic response:	Current oscillations:	Stator connection:
	Control strategy	Controller							
[41]	**DPC:**	PI	Medium	1.5 MW	++	Low	+++	Low	Grid-connection
[42]		Hysteresis	Low	2 MW	+++	Neglected	++	Neglected	Grid-Connection
[43]		Hysteresis	Low	2 MW	++	Low	++	High	Grid-connection
[44]		PI/Hysteresis	Medium	1.5 MW	++	Low	+++	Low	Grid-connection
[45]		PI/Hysteresis/FLC	Medium	1.5 MW	++	Low	+++	Low	Grid-connection & Stand-alone
[46]		PI/NN	Medium	1.5 MW	+	Low	+	Low	Grid-connection
[47]		PI/SMC/ Nonlinear controller	High	2 MW	++	Low	+++	Low	Grid-connection
[48]		PI/PI-R	Medium	2.2 KW	++	Low	+++	Low	Stand-alone
[49]	**DTC:**	ISM	High	3 KW	++	Neglected	++	-	Grid-connection
[50]		PI/Hysteresis	Low	2 MW	+++	Neglected	+++	-	Grid-connection
[51]		Hysteresis	Low	-	++	Low	++	-	Grid-connection
[52]	**BSC:**	Backstepping	High	2 MW	+++	Neglected	+++	Low	Grid-connection
[53]	**SMC:**	FOSMC	High	2 MW	+++	Medium	++	Low	Grid-connection
[38]		NSMC	High	-	+++	Neglected	+++	-	Grid-connection
[54]		HOSMC	High	1.5 MW	++	Low	++	-	Grid-connection
[55]		ADRC	High	1.5 MW	+++	Low	+++	-	Grid-connection
[56]		ISMC	High	-	+++	Low	++	Low	Grid-connection
[57]		Adaptive SMC	High	-	++	Low	+	-	Grid-connection
[58]		PI/ASMT2NFC	High	1.5 MW	+++	Neglected	+++	-	Grid-connection
[59]		STSMC	High	6 KW	+++	Neglected	+++	Low	Stand-alone
[60]	**VC:**	PI-FLC	Medium	10 KW	+++	Low	+++	Low	Grid-connection
[61]	**PDPC:**	Improved PDPC	Low	2 MW	+++	Neglected	+++	Low	Grid-connection
[19]		Hysteresis	Medium	15 KW	+++	Neglected	+++	Neglected	Grid-connection
Proposed	**DPC:**	IP	Medium	4 KW	+++	Neglected	+++	Neglected	Stand-alone

Table.13-The proposed experimental tests:

	Proposed tests
Test 01:	Rotor currents variation.
Test 02:	Sensevity to the wind speed variation.
Test 03:	Sub and Super-synchronous operation mode under fixed wind speed.
Test 04:	Power quality improvement.

Table.14-The d-q rotor current components variation (under trapezoid and step forms).

Current variation: / **Reference form**	**I_{rd}*(A) variation**	**I_{rq}*(A) variation**	**Overshoot (%)**	**Response time (ms)**	**Current error (A)**	**Tracking:**
Trapezoid form:	0 (A), -5 (A), -10 (A), -5 (A), 0 (A)	0 (A), -10 (A), -5 (A), 0 (A), -5 (A), -10 (A)	Between +0.5% and +2 %	25 (msec)	Very small +/- 0.1 A	Excellent
Step form:	0 (A), -5 (A), -10 (A), 0 (A)	0 (A), -10 (A), 0 (A), -5 (A), -10 (A), -5 (A), 0 (A)	Between +7%, 8% and 12 %)	35 (msec)	Very small +/- 0.15 A	Excellent

Table.15-The d-q rotor current components variation (for three operation zone)

Parameters: / Figures	I_{ra_meas}(A) variation	N_r(rpm) variation	Period (s)
Fig.41-(a & b)	absolute values|±| : 0 (A), 5 (A), 10 (A), 6 (A), 2 (A), 0.5 (A), 10 (A), 6 (A), 0 (A), 5(A), 0(A).	Is keeping constant = 0 rpm Speed is zero.	40 (sec)
Fig.41-(b & c)	Is keeping constant = 10 (A)	0, 1500, 1700, 1000, 1500, 1700, 1000, 500 and 0 (rpm) ⇒ (random wind speed form)	100 (sec)

Table.16-The d-q rotor current components variation (for three operation zone)

Current variation: / Mode operations	I_{rd}*(A) variation	I_{rq}*(A) variation
Sub-synchronous mode:	0 (A), -4 (A), -5 (A), 0 (A)	0 (A), -5 (A), -10 (A), 0 (A)
Synchronous mode:	0 (A), -5 (A), 0 (A)	0 (A), -5 (A), -10 (A), -2 (A), 0 (A)
Super-synchronous mode:	0 (A), -5 (A), 0 (A)	0 (A), -10 (A), -7 (A), -5 (A), -10 (A), -5 (A), -1 (A), 0 (A)

Table.17-Recapitulation results "for the three operation zones from Fig.45":

Performance: / Cases:	Zoom 1 (fig.45)				Zoom 2 (fig.45)			
	Period	Waveform	fr(Hz) and S (Slip)	Peak current (A)	Period	Waveform	Fr(Hz) and S (Slip)	Peak current (A)
Case 01: N=1000 rpm	400 m (sec)	Sinusoidal	Fr ≈ 16.67 (Hz), S=0.33	Ird*=-5 (A) Irq*=-10(A)	400 msec	Sinusoidal	Fr ≈ 16.67 (Hz), < f_S(Hz) S=0.33	Ird*=-0 (A) Irq*=-10 A⇒ 0 (A)
	Fr=1/ Trotor =1/(1.5*40 msec) =1/60 msec ≈ 16.67 Hz Fr=S*fs=((1500-1000)/1500)*50Hz ≈ 16.67 Hz							
Case 02 : N=1500 rpm	400 m (sec)	Sinusoidal	Fr=fs S ≈ 0	Ird*=-5 (A) Irq*=-10(A)	400 m sec	Sinusoidal	Fr=fs S ≈ 0	Ird*=-5 A⇒ 0A Irq*=-10 (A)
Case 03 : N=1700 rpm	10 (sec)	Sinusoidal	Fr ≈ 6.67 < f_S (Hz), S=- 0.13	Ird*=-0 (A) Irq*=-10A ⇒-7 A ⇒ -5 (A)	1 (sec)	Sinusoidal	Fr ≈ 6.67 < f_S (Hz), S=- 0.13	Ird*=-5 (A) Irq*= 0(A)

Table.18-The review of power control in Grid-connection mode (only experimental studies).

Ref	Control strategy	Current/ voltage controller	Grid nature (balanced/unbalanced)	Wind Speed m/s	Overshoot	THD (Is)	Response Time	DFIG Rated Power	Power/ current error	Robustness: Tracking reference	Robustness: To Wind speed variation	Filter type
[4]	DPC	PI	Balanced	11 m/s	/	/	/	7.5 KW	Power loss dissipation study			LC
[5]	DPC	SMC	Dip voltage	10 m/s	< 5%	< 5 %	< 10 (ms)	7.5 KW	+/-0.04 KW	++	++	/
[6]	VOC	PI	Unbalanced	/	/	/	/	15 kW	/	++	++	LC
[7]	DPC	2-SMC	Distorted grid	11 m/s	<1%	/	< 5 (ms)	4 KW	$\pm 5.10^{-3}$ KVAR =0.1%	+++	+++	/
[8]	DPC	PIR	Unbalanced	/	/	/	/	5 KW	/	++	++	L
[10]	DPC	SMC	Unbalanced	/	/	/	/	-	/	++	/	/
[12]	DPC	Hys	Balanced	/	<3 %	/	2 (ms)	3.5 KW	/	++	+++	L
[32]	FOC	Hys	Balanced	/	≈0.5% Step	≈ 3.7%	25 (ms)	3.5 KW	+/- 0.01 A	++	++	LC
[34]	DPC-VIP	VIP	Distorted grid	/	< 8 %	4.8%	40 (ms)	1 KW	/	++	++	/
[35]	LC-MPDPC	Predictive	Balanced	/	< 1%	4.13 %	1 (ms)	2 KW	/	++	++	/

Table.19-The review of power control in Stand-alone mode (only experimental studies).

Ref	Control strategy	Current/ voltage controlle	Load nature	Wind Speed	Overshoot (%)	THD (Is) %	Response Time	DFIG Rated Power	Power/ current error	Robustness		Filter type:
										Tracking reference	To Wind speed variation	
[13]	VOC	PI-R	Non-linear load	/	/	/	/	/	/	++	++	/
[14]	VOC	PR3	Nonlinear load	/	/	< 5%	< 10 (ms)	2.2 KW	/	++	++	L
[15]	FOC	Hys	Non-linear load	11.5 m/s	≈2% trapezoid	≈ 5%	30 (ms)	3.5 KW	+/- 0.01 A	++	++	LC
[16]	VOC	PI	Resistive load	16 m/s	< 8 %	< 5%	< 8 (ms)	7.5 KW	/	++	++	L
[19]	PDPC	PI	Nonlinear load	/	< 10 %	5.98%	< 15 (ms)	20 KW	/	+++	++	/
[20]	VOC	PI	Nonlinear load	/	< 7%	/	< 15 (ms)	5.5 KW	/	++	++	/
[21]	FOC	PI	Nonlinear load	/	< 10%	/	< 50 (ms)	3.2 KW	/	+++	++	/
[22]	FOC	PI	Nonlinear load	/	/	/	/	5.5 KW	/	++	++	L
[23]	FOC	PI-R	Unbalanced load	/	< 6 %	< 5%	< 10 (ms)	2.2 KW	/	+++	++	L
Proposed	DPC	IP	RL-load	13.5 m/s	≈2% trapezoid ≈8% Step	< 4%	25 (ms) 35 (ms)	4.5 KW	+/- 0.1 A	+++	++	LCL

Appendix

Table.20-Parameters of the DFIG (Simulation study).

Rated Power:	4.0 kW
Stator Resistance:	Rs = 1.2 Ω
Rotor Resistance:	Rr = 1.8 Ω
Stator Inductance:	Ls = 0.1554 H.
Rotor Inductance:	Lr = 0.1558 H.
Mutual Inductance:	Lm = 0.15 H.
Rated Voltage:	Vs = 220/380 V
Number of Pole pairs:	p= 2
Rated Speed:	N=1440 rpm
Friction Coefficient:	f_{DFIG}=0.00 N.m/sec
The moment of inertia	J=0.2 kg.m^2

Table.21-Parameters of the Turbine (Induction Machine/Simulation study).

Rated Power:	4.5 kW
Number of blades:	P= 3
Blade diameter	R= 3 m
Gain:	G=4.15
The moment of inertia	J_t=0.00065 kg.m^2
Friction coefficient	f_t=0.017 N.m/sec
Air density:	ρ=1.22 Kg/m^3

Table.22-Parameters of the DFIG (Experimental study).

Rated Power:	4.5 kW
Stator Resistance:	Rs = 0.4 Ω
Rotor Resistance:	Rr = 0.8 Ω
Stator Inductance:	Ls = 0.082 H.
Rotor Inductance:	Lr = 0.082 H.
Mutual Inductance:	Lm = 0.081 H.
Rated Voltage Δ/Y:	Vs = 220/380 V
Number of Pole pairs:	P= 2
Rated Speed:	N=1395 rpm
Friction Coefficient:	f_{DFIG}=0.001 N.m/sec
The moment of inertia	J=0.2 kg.m^2

Table.23-Parameters of the emulator turbine (Squirrel cage Induction Machine/Experimental study).

Rated Power:	4.0 kW
Rated Voltage (Vs) Δ/Y:	Vs= 220/380 V.
Cosφ:	0.82
Gain:	G=3.9
Rated Speed:	N= 1440-2000 rpm

Table.24-PI controller parameters for Vdc bus voltage (Grid Side converter)

PI parameters:	Gain values:
$Kp_{\_Vdc}$:	$1/1e^{-3}$
$Ki_{\_Vdc}$:	1

Table.25- Gain values used to design PI and IP respectively.

Gain parameters:	Gain values of PI	Gain values of IP	
	Simulation	Simulation	Experimental
K_P:	0.005	0.0011	30
K_i:	0.846	-461.78	10

Table.26-The simulation conditions using Matlab/Simulink® R2009a

Type:	Fixed-Step.
Ode-4:	Range Kutta Order4
Fixed-step Size (Fundamental sample time):	Simulation study: 1e-5.
Fixed-step Size (Fundamental sample time):	Experimental study: 1e-4.
Tasking mode for periodic sample time:	Auto.